ACS Chemical Neuroscience

Research Article

pubs.acs.org/chemneuro

Syntheses and Evaluation of Carbon-11- and Fluorine-18-Radiolabeled pan-Tropomyosin Receptor Kinase (Trk) Inhibitors: Exploration of the 4-Aza-2-oxindole Scaffold as Trk PET Imaging Agents

Vadim Bernard-Gauthier,*[,†,‡] Arturo Aliaga,[§] Antonio Aliaga,[∥] Mehdi Boudjemeline,[∥] Robert Hopewell,[∥] Alexey Kostikov,[∥] Pedro Rosa-Neto,[§] Alexander Thiel,[⊥] and Ralf Schirrmacher*[,‡,∥]

[†]Experimental Medicine, Department of Medicine, McGill University, 1110 Pine Avenue West, Montreal, Quebec H3A 1A3, Canada

[‡]Department of Oncology, University of Alberta, 11560 University Avenue, Edmonton, Alberta T6G 1Z2, Canada

[§]Translational Neuroimaging Laboratory, McGill Centre for Studies in Aging, Douglas Mental Health University Institute, 6875 Boulevard LaSalle, Montreal, Quebec H4H 1R3, Canada

[∥]McConnell Brain Imaging Centre, Montreal Neurological Institute, McGill University, 3801 University Street, Montreal, Quebec H3A 2B4, Canada

[⊥]Department of Neurology and Neurosurgery, McGill University, Jewish General Hospital, 3755 Cote St. Catherine Rd., Montreal, Quebec H2T 1E2, Canada

Supporting Information

ABSTRACT: Tropomyosin receptor kinases (TrkA/B/C) are critically involved in the development of the nervous system, in neurological disorders as well as in multiple neoplasms of both neural and non-neural origins. The development of Trk radiopharmaceuticals would offer unique opportunities toward a more complete understanding of this emerging therapeutic target. To that end, we first developed [^{11}C]GW441756 ([^{11}C]**9**), a high affinity photoisomerizable pan-Trk inhibitor, as a lead radiotracer for our positron emission tomography (PET) program. Efficient carbon-11 radiolabeling afforded [^{11}C]**9** in high radiochemical yields (isolated RCY, 25.9% ± 5.7%). In vitro autoradiographic studies in rat brain and TrkB-expressing human neuroblastoma cryosections confirmed that [^{11}C]**9** specifically binds to Trk receptors *in vitro*. MicroPET studies revealed that binding of [^{11}C]**9** in the rodent brain was mostly nonspecific despite initial high brain uptake (SUV_{max} = 2.0). Modeling studies of the 4-aza-2-oxindole scaffold led to the successful identification of a small series of high affinity fluorinated and methoxy derivatized pan-Trk inhibitors based on our lead compound **9**. Out of this series, the fluorinated compound **10** was selected for initial evaluation and radiolabeled with fluorine-18 (isolated RCY, 2.5% ± 0.6%). Compound [^{18}F]**10** demonstrated excellent Trk selectivity in a panel of cancer relevant kinase targets and a promising *in vitro* profile in tumors and brain sections but high oxidative metabolic susceptibility leading to nonspecific brain distribution *in vivo*. The information gained in this study will guide further exploration of the 4-aza-2-oxindole scaffold as a lead for Trk PET ligand development.

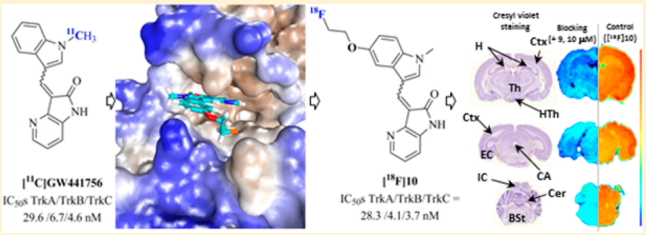

KEYWORDS: *Tropomyosin receptor kinases, positron emission tomography, imaging, tyrosine kinase inhibitor, aza-oxindole, carbon-11, fluorine-18, radiochemistry, brain imaging, neuroblastoma*

Tropomyosin receptor kinases (Trk) encompass the three highly homologous receptors TrkA, TrkB, and TrkC, which are transphosphorylated and activated upon preferential and high affinity binding with dimeric neurotrophins. Nerve growth factor (NGF) binds TrkA, brain-derived neurotrophic factor (BDNF) and neutrophin-4/5 bind TrkB, while neurotrophin-3 (NT-3) preferentially binds TrkC ($K_d \approx (1.7–2.3) \times 10^{-11}$ M).[1] All Trk proteins share an analogous sequence and common general arrangement, which includes an intracellular kinase domain connected via a transmembrane region to five consecutive extracellular domains.[2] The downstream signaling ensuing from the extracellular activation of those receptor tyrosine kinases (RTKs) with their cognate ligands supports pivotal functions in the development and maintenance of the mammalian nervous system such as synaptogenesis, neuronal differentiation, and synaptic plasticity.[3−6] Each neurotrophin also interacts with a common low affinity receptor, $p75^{NTR}$, a member of the tumor necrosis factor family ($K_d \approx 10^{-9}$ M).[7] TrkA expression, along with its cognate ligand, is extensive in

Received: August 25, 2014
Accepted: October 28, 2014
Published: October 28, 2014

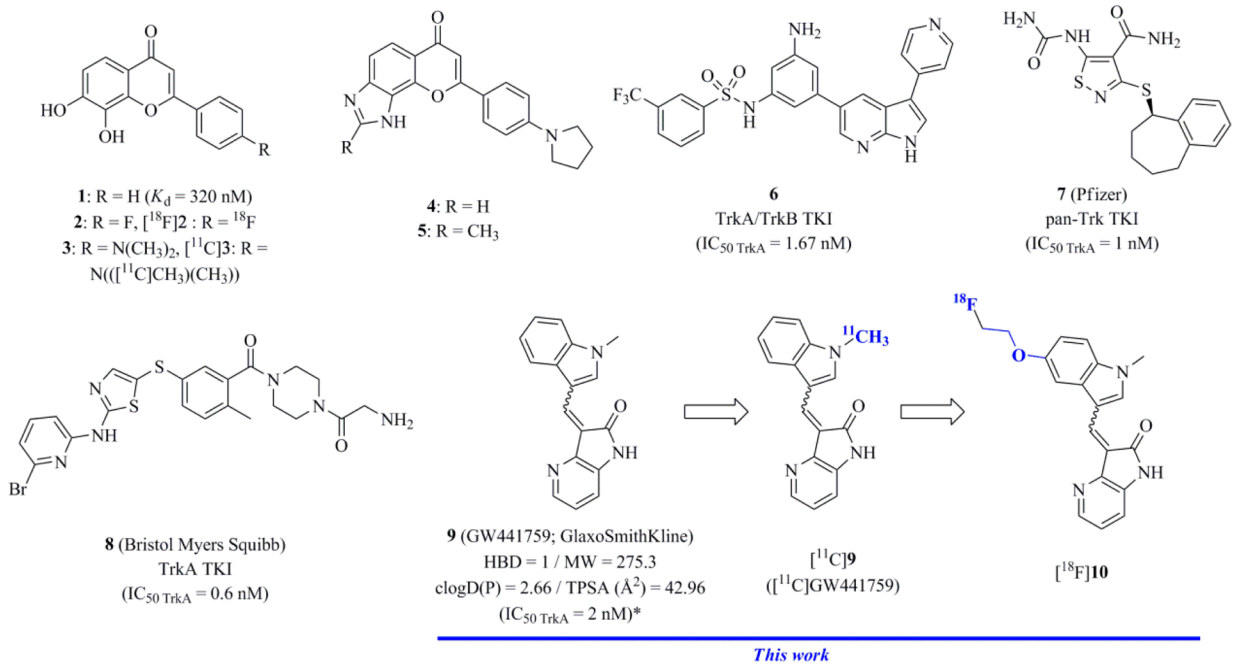

Figure 1. Chemical structures of Trk agonists, tyrosine kinase inhibitors, and Trk radioligands. *Indicates data taken from ref 41.

restricted neuronal populations such as cholinergic neurons of the basal forebrain (BFCNs) and striatum, as well as in sensory and sympathetic ganglia.[8,9] TrkB and TrkC receptors are, for their part, widely coexpressed throughout the mammalian central (CNS) and peripheral nervous system (PNS).[10,11] Outside of neural lineages, cell-type specific expression of the different Trk receptors is also found in many organs such as diverse components of the lung.[12]

Within the CNS, alterations in expression and abnormal function of NGF/TrkA and BDNF/TrkB systems have been extensively investigated and linked to various neurological diseases and conditions.[13] For example, the observation that the NGF/TrkA system crucially supports survival and differentiation in BFCNs combined with the significant cholinergic dysfunction observed in early Alzheimer's disease (AD) points toward the underlying implication of NGF/TrkA in the onset and progression of AD.[14,15] Indeed, substantial down-regulation of Trk genes has been characterized within BFCNs of the nucleus basalis (NB) in mild cognitive impairment (MCI) and, more significantly, in mild to moderate AD compared with no cognitive impairment (NCI) cases.[16] Furthermore, TrkA receptor densities in cholinergic NB neurons are diminished in MCI and AD in contrast with NCI.[17] In early stage AD, TrkA protein levels are also reduced in cortical regions, where TrkA is naturally expressed in lower concentrations compared with the basal forebrain and caudate putamen (CP).[18] Analogously, decline in cortical TrkB receptor and BDNF levels is also found in AD patients.[19] In fact, dysregulation of the BDNF/TrkB system is found in a variety of neurodegenerative/psychiatric diseases and neuropathological conditions such as Parkinson's disease (PD), Rett syndrome, Huntington's disease (HD), schizophrenia, and traumatic brain injury (TBI).[20−23] Moreover, accumulating evidence supports the critical involvement of Trk in malignant transformations, chemotaxis, anoikis resistance, metastasis, and survival signaling in various neural and non-neural human cancers including pancreatic, lung, prostate, and neuroendocrine tumors.[21−28]

Therefore, Trk receptors have been actively pursued as therapeutic targets for both neurological and oncological diseases.[29,30] The development of noninvasive *in vivo* imaging probes allowing the assessment and quantitation of Trk levels would provide an invaluable tool to evaluate Trk-related neurological and oncological conditions. Such a research tool would offer a deeper understanding of the expression and functions of those receptors within the normal, as well as pathological, nervous system. It would provide a molecular instrument for the assessment of receptor occupancy and therapeutic effects during current drug development efforts. Among available imaging techniques, positron emission tomography (PET) is particularly well suited to address these objectives owing to its high sensitivity and dynamic measurement.

Small molecules (MW < 500 Da) binding Trk receptors have been explored from two distinct perspectives. First, from a neurological standpoint, efforts have mainly been directed at compounds exerting their effect upon binding the extracellular domain (ECD) of Trk receptors.[29] This approach has relied on either random screening or neurotrophin mimicry and typically targets challenging druggable sites corresponding to clefts in protein−protein interfaces from individual Trk/neurotrophin heterodimers.[31] One of the rare examples of successful nonpeptidic EDC-binding Trk probes of this type is the TrkB-selective agonist 7,8-dihydroxyflavone (**1**, $K_d \approx 320$ nM; Figure 1) and its derivatives.[32] From an oncological perspective, applications have focused on the intracellular well-characterized kinase domain, which has led to the identification of numerous and structurally diverse potent tyrosine kinase inhibitors (TKIs).[30] Some examples of Trk-TKIs include 3,5-disubstituted 7-azaindoles **6** (TrkA IC_{50} = 1.67 nM),[33] isothiazole **7** (TrkA IC_{50} = 1 nM),[34] and 2-amino-5-(thioaryl)thiazole **8** (TrkA IC_{50} = 0.6 nM)[35](Figure 1). As a result of important kinase homology sequences of the different Trk isoforms, Trk-TKIs, including the aforementioned inhibitors, generally present limited intra-Trk selectivity profiles but often display excellent selectivity over non-Trk kinase targets.[36]

dx.doi.org/10.1021/cn500193f | ACS Chem. Neurosci. 2015, 6, 260−276

Scheme 1. Syntheses of (*Z*)-9, Photoisomerization Leading to (*Z*)/(*E*)-9 Mixtures, and ORTEP Diagrams for Compounds 12 and (*Z*)-9[a]

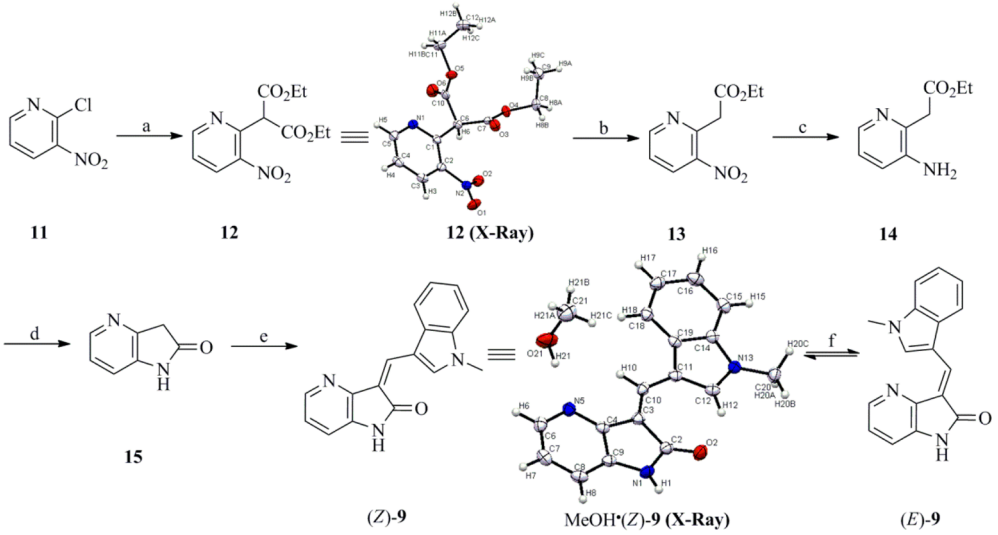

[a]Synthesis of (*Z*)-**9** and (*E*)-**9**. Reagents and conditions: (a) NaH, dimethyl malonate, DMSO, rt, 30 min, then 100 °C, 1 h (97%); (b) LiCl, H_2O, DMSO, rt to 100 °C, 18 h (98%); (c) H_2 (1 atm), Pd/C, MeOH, rt, 6 h (98%); (d) HCl_{aq} (2.0 N), Et_2O, rt, 12 h (52%); (e) 1-methylindole-3-carboxaldehyde, AcOH, HCl_{conc}, 40 °C, 12 h (65%); (f) H_2O/MeCN (1:1), visible light (ambient conditions). Single-crystal X-ray structure of **12** and MeOH·(*Z*)-**9**; ellipsoids drawn at 70% probability.

Our group has recently reported the radiosyntheses of the first radiotracers aimed at Trk PET imaging.[37] The probes evaluated, 4′-[^{18}F]-7,8-DHF ([^{18}F]**2**) and 4′-([*N*-methyl-^{11}C]-dimethylamino-7,8-DHF ([^{11}C]**3**) (Figure 1), are derivatives of 7,8-dihydroxyflavone (**1**). Despite promising *in vitro* autoradiographic profiles paralleling [^{125}I]-BDNF assays[38] and showing BDNF-competitive binding, the tracers were subject to rapid hepatic *in vivo* metabolism caused by the catechol moiety and were consequentially found unsuitable for PET brain imaging. While bioisosteric modifications of those EDC-binding tracers are currently underway, we aimed at accessing Trk receptors via the intracellular kinase domain with radiolabeled TKIs. Because the ultimate goal of this project is the development of PET tracer candidates for both peripheral tumor and central nervous system imaging, our probe identification efforts were focused on TKIs with narrowed physicochemical properties such as (1) blood−brain barrier (BBB) permeation and neuroreceptor imaging binding potential (ideally BP = B_{max}/K_d > 10), (2) molecular weight (MW) ≤ 305, (3) calculated distribution coefficient ($cLogD_{7.4}$) in the range of 2.0−3.5, (4) topological polar surface area (TSPA) of 30−80 Å^2, and (5) hydrogen bond donor (HBD) ≤ 1.[39,40] Based on those and other crucial considerations such as radiolabeling compatibility, we selected 3-((1-methyl-1*H*-indol-3-yl)methylene)-1*H*-pyrrolo[3,2-*b*]-pyridin-2(3*H*)-one (GW441756, **9**)[41] from an initial screening of over 100 reported Trk-TKIs. 4-Aza-2-oxindole **9** displays favorable physicochemical properties for BBB permeation (Figure 1) and high TrkA affinity (IC_{50} = 2 nM) leading to theoretical binding potentials up to BP > 6.6 in TrkA-rich brain regions (B_{max}= 13.2 fmol mg^{-1} tissue in rat CP).[42] Also, **9** displays >100 fold selectivity over off-target tested kinases[41] and, importantly, can be readily converted into a radiolabeled *N*-[^{11}C]-methyl isotopologue for *in vivo* PET imaging.

In the present study, the development of the 4-aza-2-oxindole Trk-binding tracer [^{11}C]**9** is described, including the syntheses of (*Z*)-**9** along with the desmethyl precursor (*E*)-**16**, their intrinsic isomerization properties, and a molecular modeling investigation. Results from biological evaluations are provided including the *in vitro* enzymatic activity of **9** for all Trk receptors (TrkA, TrkB, and TrkC), rat brain and human neuroblastoma *in vitro* autoradiography studies of [^{11}C]**9**, metabolic studies, and microPET imaging experiments, demonstrating that [^{11}C]**9** readily crosses the BBB but binds nonspecifically in the rat brain. Furthermore, a series of novel highly potent 4-aza-2-oxindole-based Trk inhibitors amenable for ^{11}C- or ^{18}F-radiochemistry are described. This effort led to the synthesis of [^{18}F]**10**, which demonstrates a promising *in vitro* profile. The tracer [^{11}C]**9** is the first brain penetrating Trk radioligand described, and these results suggest that 4-aza-2-oxindoles represent a potentially versatile scaffold for further development of PET Trk probes.

RESULTS AND DISCUSSION

Synthesis and Photoisomerization of (*Z*)-9. Inhibitor **9** belongs to the family of 3-arylideneindolin-2-one RTK inhibitors with antioncogenic properties.[43] Typically the arylidene fragment in these structures is incorporated via base-catalyzed or acid-promoted aldehyde condensation with a suitable indolin-2-one intermediate. In the present case, we synthesized the required precursor 4-aza-indoline-2-one (**15**) in four steps and 48% overall yield from 2-chloro-3-nitropyridine (**11**) as previously described but without detailed instructions and characterization (Scheme 1).[41] Intermediate **12** was also characterized by single molecule X-ray crystallography.

The exocyclic olefin can adopt a strict *Z* conformation or *E* conformation or exists as a *Z*/*E* mixture, depending on the nature of the arylidene fragment in 3-substituted indolin-2-ones.[44] Increased inhibitory activities for various kinases have previously been reported for compounds preferentially adopting the *Z* conformation.[43b,d,44] Initial synthesis of **9** by Wood et al.[41] described the isolation of a crude 8:1 mixture of nonspecified isomeric composition. In our experiments, the condensation of **15** with 1-methylindole-3-carboxaldehyde in glacial acetic acid and concentrated HCl at 40 °C gave **9** as a

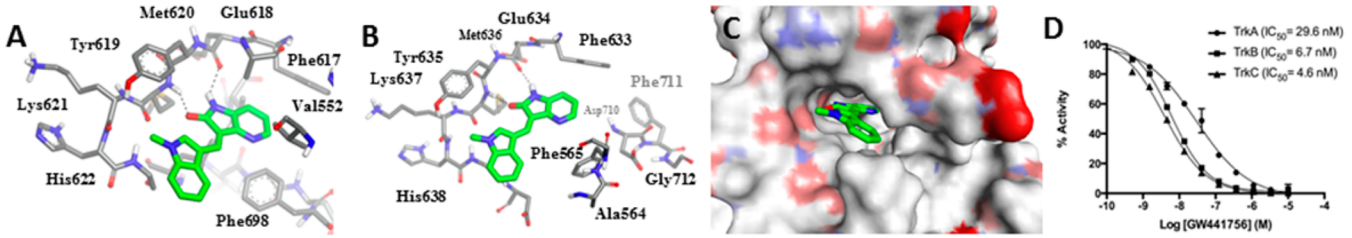

Figure 2. Comparison of the predicted binding poses for (*Z*)-**9** bound to (A) TrkC (PDB code 3V5Q) with a DFG-out binding mode and to (B, C) TrkB (PDB code 4AT3) and with a DFG-in binding mode. The lactam moiety of (*Z*)-**9** forms H-bonding interactions with Glu634 and Met636 from TrkB and Glu618 and Met620 from TrkC. The coloring of the protein surface emphasizes positive, neutral, and negative atom charge (red, white, and blue, respectively). (D) Dose−response curves and comparison of IC_{50} values for the *in vitro* kinase assays with **9** (GW441756) versus TrkA, TrkB, and TrkC. The inhibitor (**9**) was tested at ten different concentrations using serial dilution, experiments were carried out in duplicate in the presence of 1 μM of ATP, and error bars represent standard deviation from the mean.

single isomer in 65% yield after flash chromatography (Scheme 1). This compound was identified as the *Z* isomer based on the characteristic ^{1}H NMR downfield chemical shift (9.48 ppm) corresponding to the H-2′ proton in proximity to the carbonyl group.[43a,44] This assignment was unambiguously confirmed by single molecule X-ray crystallography elucidation of the planar (*Z*)-**9**−MeOH adduct (Scheme 1). Mechanistically, the preferential formation of the *Z* isomer under the reaction conditions used can be rationalized considering the least sterically hindered transition state of the stabilized β-hydroxyketone intermediate, which ultimately dictates the orientation of the arylidene moieties relative to the 4-azaoxindole core (Scheme S1, Supporting Information). Despite the isolation of the pure crystalline (*Z*)-**9**, we observed under various conditions rapid photoisomerization leading to the formation of a mixed-isomer photostationary state (PSS) of equimolar *E*/*Z* composition (Figure S1, Supporting Information). The *N*-desmethyl radiolabeling precursor **16** for ^{11}C-radiomethylation was then synthesized in good yields following the procedure used for preparing (*Z*)-**9** (Figure 3A). Interestingly, this product was obtained as the pure *E* isomer based on the H-2′ proton ^{1}H NMR peak found at 10.02 ppm (Figure S2, Supporting Information). This structural assignment is in agreement with previous NMR characterization of 3-subsituted 4-azaindolin-2-ones derivatives.[43a] We hypothesized that the isolation of (*E*)-**15** was the consequence of a base-promoted isomerization during the workup procedure. Despite the fact that it should be expected that the inhibitory activity of **9** arises from the interaction of the *Z* isomer with the ATP binding pocket (*vide infra*), we anticipated that the radiomethylation of (*E*)-**16** would release [^{11}C]**9** as a ∼1:1 *E*/*Z* mixture owing to the rapid photoisomerization irrespective of the isomeric composition of the precursor.

***In Vitro* Binding Assays.** Our focus on **9** as a potential radiotracer originated from the early work by Wood et al., which demonstrated that **9** displays a 2 nM IC_{50} for TrkA inhibition and >100-fold selectivity for TrkA over a panel of receptor tyrosine kinases (C-FMS, ITK, VEGFR2), non-receptor tyrosine kinases (SRC), mitogen-activated kinases (CDK1, CDK2, JNK3, p38, ERK), and histidine kinases (PDHK4).[41] Yet, all Trk inhibitors characterized to date only display at best marginal intra-Trk selectivity since the three Trk isoforms share between 71.9% and 78.3% of their kinase domain and between 95% and 100% residue identity when considering only the 40 amino acids that are potentially involved in ligand binding from the DFG-in ATP binding site.[45] Therefore, we sought to evaluate the ability of MeOH·(*Z*)-**9** to inhibit the entire human Trk receptor family, TrkA, TrkB, and TrkC. Hence, the compound MeOH·(*Z*)-**9** was tested in a radiolabeled ATP-based *in vitro* enzymatic assay and was shown to inhibit TrkA with an IC_{50} of 29.6 nM and to be 4- and 6-fold more potent against TrkB and TrkC, respectively (IC_{50TrkB} = 6.7 nM and IC_{50TrkC} = 4.6 nM) (Figure 2D). Although the specific isomeric composition responsible for the observed *in vitro* inhibition could not be determined, our previous photoisomerization study suggests that it was derived from a near equimolar *E*/*Z* mixture (in dilute solutions).

Molecular Docking Study of Compound 9. In order to gain insight into the putative binding modes of **9** and indications for potential positions for eventual structural modifications, a docking study was performed using the FITTED program.[46] Assessment of the differences in the binding poses of (*Z*)-**9** and (*E*)-**9**, as well as the influence of the activation state of the kinase domain on binding, was first conducted. Accordingly, we selected the available crystal structures of (1) the activated (DFG-in) TrkB kinase domain (PDB code 4AT3) and (2) the inactivated (DFG-out) TrkC kinase domain (PDB code 3V5Q). Docking of (*Z*)-**9** on both proteins converged on analogous binding poses anchoring the ligand via H-bonding interactions between the lactam proton with Glu634 or Glu618 and the carbonyl oxygen atom with Met636 or Met620 in TrkB and TrkC, respectively (Figure 2A−C). Edge-to-face stacking interactions are also present between the pyridine ring and the gatekeeper Phe633 (TrkB) and Phe617 (TrkC). This binding mode does not involve interactions with the DFG motif and is overall consistent with most available 3-arylideneindolin-2-one-based ligands cocrystallized with various kinases (DFG-in),[47] as well as TrkC (DFG-out).[36] On the other hand, attempts to dock (*E*)-**9** did not convincingly generate adequate binding modes with TrkB and TrkC, presumably due to unfavorable protein contacts between the 1-methylindole and Phe565 in TrkB (DFG-in) and Phe698 in TrkC (DFG-out) (Figure 2A,B). An alternative binding mode, which brings the 1-methylindole fragment into the vicinity of Phe589, could be obtained from the docking of (*E*)-**9** with TrkA (PDB code 4AOJ) (Figure S3, Supporting Information), but this binding mode within the ATP binding site has only been rarely encountered in cocrystal structures and is associated with low affinity ligands.[48]

As expected, the binding pose of (*Z*)-**9** with TrkA corroborates the previously modeled TrkB− and TrkC−(*Z*)-**9** interactions (Figure S4B, Supporting Information). The docking information also exposed small discrepancies in noncovalent interactions between TrkA and TrkB/TrkC that may account for the moderate selectivity of **9** for the latter (see Supporting Information, Figure S4). Taken together, these

dx.doi.org/10.1021/cn500193f | *ACS Chem. Neurosci.* 2015, 6, 260−276

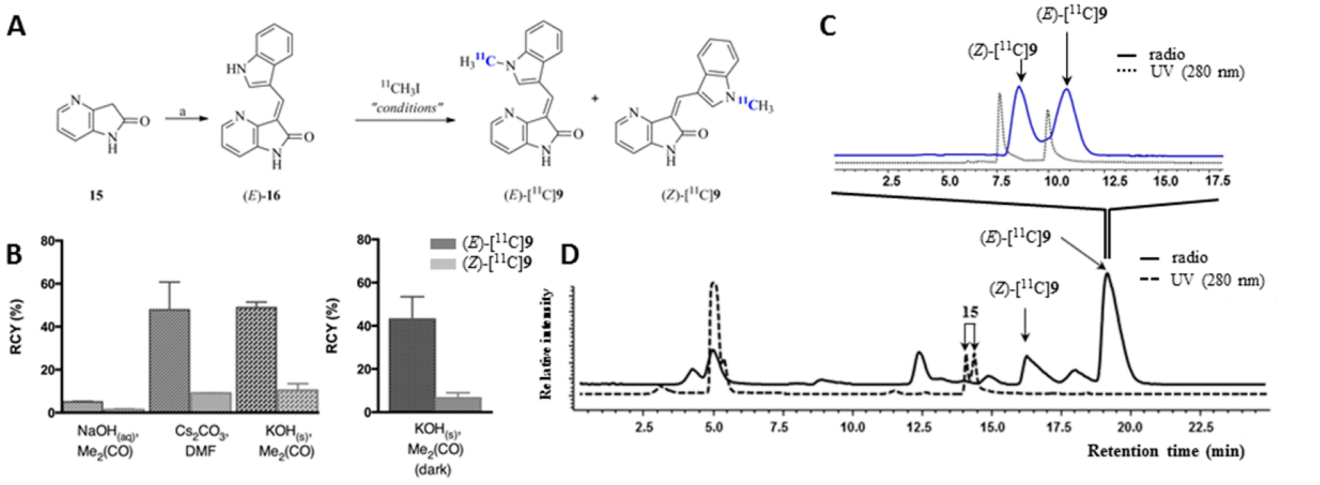

Figure 3. Synthesis of precursor (*E*)-**16** and radiosyntheses of (*Z*)-[^{11}C]**9** and (*E*)-[^{11}C]**9**. (A) Reagents and conditions: (a) indole-3-carboxaldehyde, AcOH, HCl_{conc}, 40 °C, 12 h. (B) Optimization for the radiosynthesis of (*Z*)-[^{11}C]**9** and (*E*)-[^{11}C]**9**; the RCYs are calculated by radio-HPLC and reported as the RCY ± SD (%) (ndc) from two independent experiments. Reagents and conditions: 1.0 mg of precursor (*E*)-**15** in 250 μL of solvent; (left) (i) $NaOH_{(aq)}$ (4.0 N, 5.0 μL); (ii) Cs_2CO_3 (10 mg); (iii) $KOH_{(s)}$ (10 mg); (right) (i) $KOH_{(s)}$ (10 mg), no light. (C) HPLC radiodetection QC of the collected (*E*)-[^{11}C]**9** peak at time of microPET injection showing racemization (HPLC method D). The dashed line corresponds to the UV trace of (*Z*)-**9** and (*E*)-**9** (0.7 min calibrated delay between UV and radioactivity detector). (D) HPLC separation of (*Z*)-[^{11}C]**9** and (*E*)-[^{11}C]**9** from (*E*)-**15** (HPLC method B).

results support the hypothesis that Trk inhibition of **9** involves the binding of the *Z* geometric isomer within the ATP binding site and provide reasonable details to explain the observed differences in IC_{50}'s.

Radiolabeling of [^{11}C]9. Radiolabeling of (*E*)-**16** was performed by reacting the precursor with [^{11}C]methyl iodide ([^{11}C]CH_3I), obtained from reduction/iodination of cyclotron-produced [^{11}C]CO_2, in either DMF or acetone in the presence of a suitable base (Figure 3A,B). Optimization reactions were carried out in duplicate at room temperature for 5 min. Initial radiomethylation attempts with minute amounts of aqueous NaOH in acetone only yielded (*E*)-[^{11}C]**9** with 5.0% ± 0.3% radiochemical yield (RCY, HPLC-based and non-decay-corrected, ndc). However, the labeling was found to be highly efficient in the presence of either Cs_2CO_3 in DMF or solid KOH suspended in acetone. Under those conditions, (*E*)-[^{11}C]**9** was obtained in 48% ± 13.0% and 49% ± 2.5% RCY (HPLC-based and non-decay-corrected), respectively. Radiomethylation in the presence of stronger bases such as NaH or *t*-BuOK in THF only resulted in radioactive side-product formation. Reactions leading to the formation of (*E*)-[^{11}C]**9** also afforded non-negligible and consistent amounts of (*Z*)-[^{11}C]**9** corresponding to 0.23 ± 0.06 of the *E* isomer (HPLC-based and non-decay-corrected, Figure 3B,D). Considering the low pK_a of the N−H indole moiety in (*E*)-**16** (pK_a < 12),[49] we hypothesize that the radiomethylation quantitatively proceeds via the highly conjugated potassium (cesium) enolate azatriene intermediate (Figure S5A, Supporting Information). Thus, the isomeric ratio of the ^{11}C-labeled end products likely reflects the proportion of 3-8′-s-*cis* and 3-8′-s-*trans* intermediates and not the isomeric composition of the precursor. Moreover, the formation of (*Z*)-[^{11}C]**9** was not the result of a light-induced isomerization of the (*E*)-[^{11}C]**9** product, because the labeling reactions performed in light-protected conical vials with the identical KOH/acetone conditions resulted in similar RCYs and *Z*/*E* ratios (Figure 3B). Moreover, the quantitative formation of a strongly conjugated anionic intermediate was confirmed by the UV−visible absorbance spectra of (*E*)-**16**, which undergoes a characteristic and rapid bathochromic shift of around 50 nm in the presence of NaOH under labeling conditions in water (Figures S5 and S6, Supporting Information).[49]

Therefore, the tracer [^{11}C]**9** could easily be obtained as a *E*/*Z* (1:1) mixture as anticipated. Reverse-phase HPLC purification and collection of the *E* isomer peak afforded (*E*)-[^{11}C]**9** in 26% ± 5.7% (n = 8) RCY ndc (based on starting activity of [^{11}C]CH_3I), which within the time required for sterile medium formulation for imaging studies (t ≈ 5 min), reached a PSS composed of approximately equimolar quantities of both *Z* and *E* isomers as expected (Figure 3C). The formulated tracer was obtained in >98% radiochemical purity and specific activities ranging from 29.6 to 59.2 GBq/μmol at the end of synthesis in a procedure of approximately 60 min from bombardment and was stable for over 60 min at room temperature.

***In Vitro* Metabolism of [^{11}C]9.** Tracer [^{11}C]**9** (mixed isomers) was highly stable in rat plasma *in vitro*. No significant decomposition was observed by reverse phase radio-HPLC upon incubation for 60 min at 37 °C (>99% [^{11}C]**9** unchanged). In addition, *in silico* predictions of the phase I cytochrome P450 (CYP) mediated sites of metabolism (SoM) were carried out using IMPACTS.[50] This study provided the top two predicted sites of oxidation (Figure 4) and transition state modeling (Figure S7, Supporting Information) for a set of

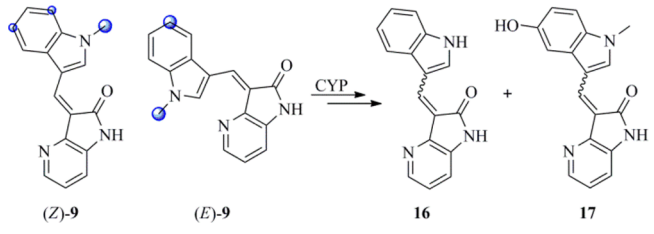

Figure 4. *In silico* top predicted CYP-mediated sites of metabolism for (*Z*)-**9** and (*E*)-**9** and corresponding metabolites confirmed by RLM assays.

dx.doi.org/10.1021/cn500193f | ACS Chem. Neurosci. 2015, 6, 260−276

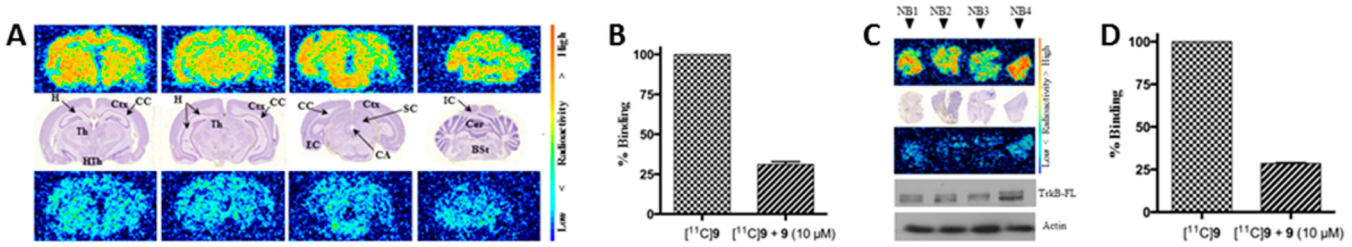

Figure 5. (A) Representative *in vitro* autoradiography in four representative coronal sections of rat brain. (upper row) Autoradiography images showing the binding of [^{11}C]**9** alone. (middle row) Cresyl violet staining of the corresponding coronal sections. BSt = brain stem; CA = cerebral aqueduct; CC = corpus callosum; Cer = cerebellum; Ctx = cortex; EC = entorhinal cortex; H = hippocampus; HTh = hypothalamus; IC = inferior colliculus, SC = superior colliculus; Th = thalamus. (lower row) Autoradiography images showing the binding of [^{11}C]**9** in co-incubation with unlabeled **9** (10 μM). (B) Quantitative results of blocking experiments with brain sections. (C) In vitro autoradiography of four representative sections from four human neuroblastoma tumors. Autoradiography images showing the binding of [^{11}C]**9** alone, cresyl violet staining of the corresponding sections, and binding of [^{11}C]**9** in co-incubation with unlabeled **9** (10 μM). Western blots analysis of the TrkB (FL, full length) protein levels. Actin was used as loading control. (D) Quantitative results of blocking experiments from human neuroblastoma tumor cryosections. Value expressed as mean ± SD (from the average of 10 sections from three rat brains and from four tumors with two sections analyzed each).

five CYP isoenzymes responsible for 90% of xenobiotic metabolism in human (CYP1A2, CYP2C9, CYP2D6, CYP3A4, and CYP2C19).[51]

The 1-methylindole carbon (C′-1) was identified as the main SoM over the entire set of CYP evaluated for both (*Z*)-**9** and (*E*)-**9**. Aromatic hydroxylations at C-5′ and C-7′ were also predicted. *In vitro* microsomal assays with rat liver microsome (RLM) and the nonradioactive inhibitor **9** (*E*/*Z* mixture) were consistent with the computational predictions and confirmed that phase I metabolism preferentially led to the slow formation of desmethyl metabolite **16** (over 90 min). HPLC analysis at various time points also revealed the formation of a minor and more polar metabolite consistent with a hydroxylated metabolite (peak A, Figure S8, Supporting Information).

***In Vitro* Autoradiography of [^{11}C]9.** Binding of [^{11}C]**9** in the brain was assessed using *in vitro* autoradiography with rat brain slices (n = 3) over successive coronal sections (n = 10). Nonspecific binding was evaluated by co-incubation with excess of the corresponding nonradioactive ligand. Figure 5A illustrates representative autoradiograms of brain slices after incubation with [^{11}C]**9** and blocking experiments along with the histological staining of the immediately adjacent sections. The radiotracer displays widespread displaceable binding to essentially all areas of the forebrain, midbrain, and hindbrain including the neocortex, striatum, thalamus, hippocampus, and cerebellum with the exception of white matter. The extensive binding distribution of [^{11}C]**9** is in agreement with the near ubiquitous expression of TrkB and TrkC in the mammal brain as assessed by mRNA *in situ* hybridization and [^{125}I]BDNF, [^{125}I]NT-4/5, and [^{125}I]NT-3 binding studies.[38] Binding in the whole brain was uniformly reduced by 69.2% ± 1.5% (n = 30 sections) upon co-incubation with excess of **9** (10 μM, Figure 5B). Moreover, the lack of preferential binding in the caudate putamen suggests that [^{11}C]**9** does not preferentially bind to TrkA. This result is in line with the IC_{50} values obtained, which showed moderate selectivity for TrkB/C (*vide supra*). The binding to TrkB and TrkC is also supported by the superior receptor densities of those isoforms compared with TrkA in virtually all brain regions including the caudate putamen, B_{max}([^{125}I]NT-3) = 26 fmol mg^{-1} tissue versus B_{max}([^{125}I]-NGF) ≤ 13.2 fmol mg^{-1} tissue.[52] It is likely that non-displaceable binding during blocking experiments ensued in part from off-Trk but kinase-specific interactions.

Owing to the critical role of Trk receptors in various neoplasms,[21−28] we sought to investigate the potential of [^{11}C]**9** for tumor imaging. In neuroendocrine tumors and neuroblastomas in particular, heterogeneous expression of Trk is strongly predictive of clinical outcomes, TrkB and BDNF being highly expressed in aggressive tumors with poor prognoses.[53] Figure 5C shows representative autoradiograms of four human neuroblastoma samples after incubation with [^{11}C]**9** in identical conditions as previously used for brain samples along with the corresponding histological staining. Binding of [^{11}C]**9** was highly heterogeneous and significantly reduced upon co-incubation with **9** (Δ = −71.3% ± 0.3%, n = 4; Figure 5C,D). To confirm TrkB expression in the tumor samples, Western blot analysis was performed with homogenate of each tumor.

***In Vivo* PET Imaging of [^{11}C]9 in Rats.** By microPET imaging, [^{11}C]**9** was preliminary evaluated in Sprague−Dawley rats to determine brain permeation and *in vivo* distribution. In a brain scan at baseline, the tracer rapidly crossed the BBB, peaked at a maximum of 2.0 SUV (standardized uptake value) in the whole brain within 30 s, then decreased rapidly over the remaining 60 min of scanning as depicted by the time−activity curve in Figure 6A. Regional brain distribution was uniform as could be expected from the near ubiquitous Trk expression in the CNS. A second imaging experiment conducted to assess the specific binding of [^{11}C]**9** where unlabeled inhibitor **9** was administered 15 min prior to tracer injection (1 mg/kg, iv) demonstrated that the uptake of [^{11}C]**9** in the rat brain was essentially nonspecific. The somewhat higher brain uptake in the pretreatment study may imply saturation of peripheral receptors while the similarly fast kinetics in baseline/blocking studies show that brain clearance overwhelms Trk-specific binding in the brain during the time of scanning. In another experiment, a thoracic/abdominal PET scan revealed hepatobiliary clearance of the tracer as well as an important uptake of radioactivity in the lungs in agreement with high pulmonary Trk-receptor concentrations (Figure 6B).[54] Pretreatment with unlabeled **9** (1 mg/kg, iv 15 min prior to [^{11}C]**9** injection) resulted in a marked reduction of the radioactivity uptake in the lungs compared with baseline, from 4.9 to 1.6 SUV at 1 min and from 0.4 to 0.1 SUV at 55 min. Blocking also resulted in a more pronounced renal radioactivity uptake.Those observations support the additional evaluation of [^{11}C]**9** in nonrodent species due to known drug pharmacokinetics interspecies differences, as well as a derivatization into a radiolabeled tracer with a longer physical half-life (e.g., fluorine-18).

dx.doi.org/10.1021/cn500193f | *ACS Chem. Neurosci.* 2015, 6, 260−276

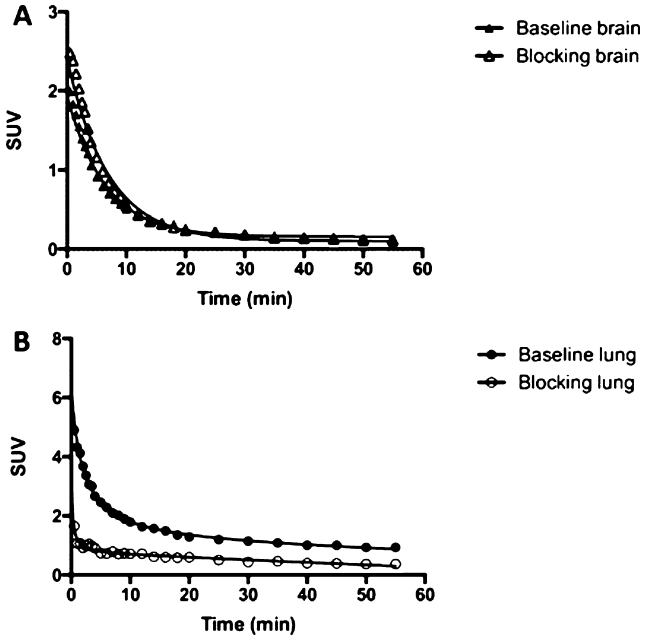

Figure 6. PET studies in Sprague–Dawley rats. Time–radioactivity curves (TACs) illustrate the accumulation of [^{11}C]**9** in (A) the whole brain and (B) the lungs as a function of time for baseline studies and for pretreatment studies with **9** (1 mg/kg, iv 15 min prior to [^{11}C]**9** injection). SUV, standardized uptake value.

Design, Syntheses, and Structure–Activity Relationship (SAR) of 4-Aza-2-Oxindole Derivatives toward ^{18}F-Labeling. On the basis of our previous results with [^{11}C]**9**, the possibilities of potential derivatives of ^{18}F-labeled analogues of **9** were explored. The selected structural alterations were chosen based on molecular modeling information from the interaction of **9** with TrkB/C (Figures 2A–C and 7A) and their accessibility as carbon-11 and fluorine-18 isotopologues. The solvent exposed phenyl moiety from the indole core of **9** appeared to provide derivatization opportunities and was therefore explored. In particular, introduction of methoxy or 2-fluoroethoxy fragments (selected for radiolabeling purposes) at positions C4′ and C5′ seemed to potentially allow additional interactions either directly or via water-mediated contacts with Asp624 (TrkC) or Asp640 (TrkB) as exemplified by docking simulations (Figure 7B,C). The 2-fluoroethoxy substitution at C6′ position appeared more problematic owing to the close proximity of Arg598, Lys643, and Lys627 in TrkA, TrkB, and TrkC, respectively. Despite being the most straightforward modification, the introduction of a 2-fluoroethyl moiety at the *N*-1′ position of the indole fragment seemed disfavored compared to **9** due to repulsive interactions with the proximal backbone of the hinge forcing a gauche conformation bringing the fluorine substituent into close proximity with residues from the glycine rich loop for all TrkA/B/C receptors (Figure 7D,E). Still, to corroborate our binding model, the *N*-fluoroethyl derivative was included in the small series of synthesized derivatives (Scheme 2, Table 1). The syntheses of compounds **10** and **18a–e** relied on the same approach as described for **9** using suitable indole-3-carboxaldehyde building blocks (Scheme 2A). The intermediates **22a,b** were prepared from the C5′/C6′-OMe precursors via BBr_3-promoted deprotection in high yields, and compounds **20** and **23a,b** were obtained via alkylation with 2-fluoroethyl 4-methylbenzenesulfonate (Scheme 2B,C; Supporting Information).

The synthesized derivatives, as well as the previously used desmethyl compound **16**, were tested for TrkA/B/C receptor binding. Table 1 lists IC_{50} values, isolated isomeric compositions, selected isomerization studies, and physicochemical properties. Compounds having an N-alkylated indole

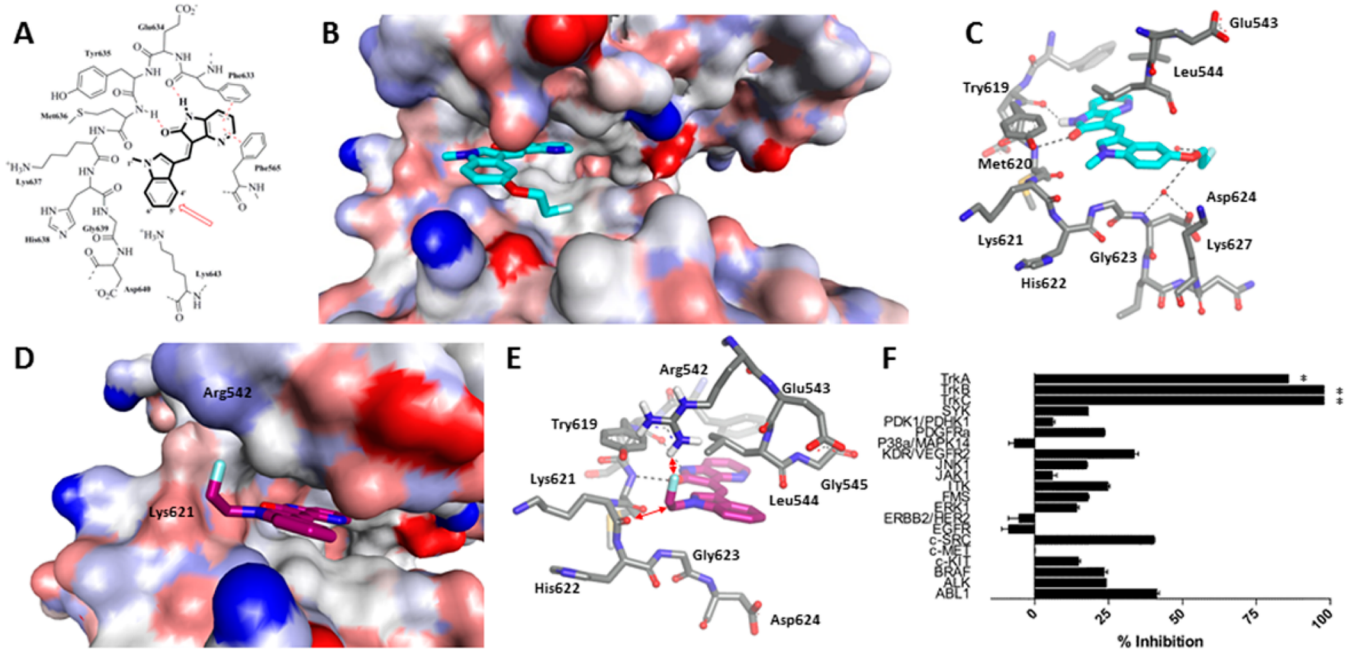

Figure 7. Design rationale and docking modes for 4-aza-oxindole-based Trk inhibitors. (A) Potential binding site interaction between TrkB and inhibitor (*Z*)-**9** based on docking studies. (B, C) Overviews of the predicted binding pose of fluorinated (*Z*)-**10** in the ATP-binding site of TrkC (PDB code 3V5Q). (D, E) Overviews of the predicted binding pose of (*Z*)-**18d** in the ATP-binding site of TrkC. The coloring of the protein surface emphasizes positive, neutral, and negative atom charge (red, white, and blue, respectively). (F) Inhibitory activity of **10** on 18 kinases at 500 nM (n = 2). * indicates that data were derived from IC_{50} curves.

dx.doi.org/10.1021/cn500193f | *ACS Chem. Neurosci.* 2015, 6, 260–276

Scheme 2. Syntheses of 3-((1-Methyl-1*H*-indol-3-yl)methylene)-1*H*-pyrrolo[3,2-*b*]pyridin-2(3*H*)-ones[a]

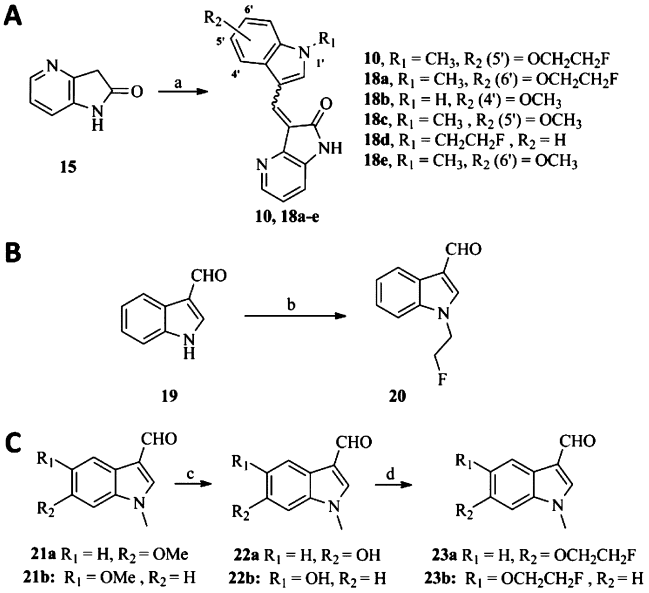

[a]Reagents and conditions: (a) indole-3-carboxaldehyde fragment, AcOH, HCl_{conc}, 40 °C, 12 h (43−72%); (b) NaH, 2-fluoroethyl 4-methylbenzenesulfonate, THF, 0 °C to rt, 12 h (96%); (c) BBr_3, CH_2Cl_2, 0 °C to rt, 3 h (94−100%); (d) K_2CO_3, 2-fluoroethyl 4-methylbenzenesulfonate, DMF, 70 °C, 12 h (72−80%).

position were isolated as *Z* isomers, while the nonalkylated compound **18b** bearing a highly acidic indole proton was, as shown with **16** previously, obtained as the *E* configurational isomer (*vide supra*). Configuration assignment was based on our previous X-ray structure determination in combination with the characteristic ^{1}H NMR signal from *E* and *Z* isomers as described earlier (see also Figures S9 and S10, Supporting Information). NMR-based photoisomerism analysis for selected inhibitors confirmed that visible light exposure results in PSS formation of different isomeric compositions (Table 1). To our satisfaction and in agreement with modeling studies, all substitutions were well tolerated except for the *N*-fluoroethyl inhibitor **18d**, which was characterized by a marked decrease in potency compared with the lead (IC_{50} = 660 nM for TrkA, IC_{50} = 108 nM for TrkB, and IC_{50} = 45.9 nM for TrkC). The presence of an OMe or fluoroethoxy group at position C5′ and C6′ had a negligible to modestly favorable impact on potency compared with **9**, except in the case of the C6′-fluoroethyoxy inhibitor **18a** as expected (IC_{50} = 62.1 nM for TrkA, IC_{50} = 10.1 nM for TrkB, and IC_{50} = 9.1 nM for TrkC). Replacement of the *N*-methyl fragment by an NH group negatively affected potency for all Trk receptors (especially TrkB) for compound **16** but increased the potency when combined with the 4′-OMe substitution in **18b**, suggesting that the loss of van der Waals interactions at the *N*-1′ position may be compensated by additional hydrogen bonding permitted through the oxygen of the C4′ substituent. It is also important to bear in mind that small discrepancies in potency may ensue from different fractions of *Z*-isomer in the PSS of those inhibitors that could not be characterized in detail for the enzymatic assay. All inhibitors displayed modest 6−15-fold inter-Trk selectivity (TrkC ≈ TrkB > TrkA). Considering those results, compound **10** was selected for radiotracer development as the most favorable fluorinated derivative in the series (cLogP = 2.87; TPSA = 56.16 Å^2; IC_{50} = 28.3 nM for TrkA, IC_{50} = 4.1 nM for TrkB, and IC_{50} = 3.4 nM for TrkC; B_{max}/IC_{50} = 6.3 for TrkB/C; see Table 1).

Prior to its conversion into a potential PET tracer, a more detail description of the selectivity profile of **10** was sought (Figure 7F). The compound was therefore tested for inhibitory activity at 500 nM concentration with a panel of 18 cancer-related kinases with an additional focus on kinase targets expressed at high concentration in neurons and various components of the mammalian CNS under nonpathological conditions.[55−59] Kinases tested were focused on closely related tyrosine kinases (TK) but also encompassed kinases from other major branches (TLK, CMGC, and AGC). Inhibitor **10** demonstrated excellent specificity and >120-fold greater potency for TrkB/C and >15-fold greater potency for TrkA compared with all other tested kinases (ABL1, ALK, BRAF, c-KIT, c-MET, c-SRC, EGFR, ERBB2/HER2, ERK1, FMS, ITK, JAK1, JNK1, KDR/VEGFR2, P38a/MAPK14, PDGFRa, PDK1/PDHK1, and SYK; tested at Reaction Biology Corporation).

Radiolabeling of [^{18}F]10. The radiolabeling of [^{18}F]**10** was achieved using a two-step procedure involving the synthesis of 2-[^{18}F]fluoroethyl tosylate ([^{18}F]FETos)[60] followed by the fluoroalkylation of precursor (*Z*)-**24** under basic conditions (Scheme 3). The phenolic precursor (*Z*)-**24** was obtained and characterized as previously described for analogous structures (vide supra). Azeotropic drying of anionic fluorine-18 and

Table 1. Potency and Physicochemical Data for 4-Aza-2-oxindole Trk Inhibitors

				IC_{50} (nM)[c]					
compd	clogP[a]	TPSA (Å^2)[a]	% of *Z* isomer[b]	TrkA	TrkB	TrkC	B_{max}/IC_{50} (TrkA)[d]	B_{max}/IC_{50} (TrkB/C)[d]	TrkC selectivity (over TrkA)
9	2.66	42.96	100/56/*e*	29.6	6.7	4.6	0.5	3.9	6.4
16	2.48	57.78	<1/*e*/*e*	103	34.0	10.9	0.1	0.8	9.4
10	2.87	56.15	>99/95/40	28.3	4.1	3.4	0.5	6.3	8.3
18a	2.87	56.15	100/*e*/*e*	62.1	10.1	9.1	0.2	2.9	6.8
18b	2.39	70.80	0/*e*/*e*	15.1	1.4	2.0	0.9	18.6	7.6
18c	2.48	59.90	100/97/24	16.3	1.7	2.1	0.8	12.4	7.8
18d	2.69	46.92	100/*e*/*e*	660	108	45.9	0.02	0.6	14.4
18e	2.48	59.90	100/*e*/*e*	71.9	6.3	4.7	0.2	5.5	15.3

[a]Values were computed with the program Pallas 3.7 for Windows (CompuDrug; SanFrancisco, CA). [b]The % of *Z* isomer was calculated based on the ratio of the diagnostic ^{1}H NMR H-2′ peak at isolation (*t* = 0 min) in d_6-DMSO and after ambient light incubation in d_6-DMSO/D_2O (5:1) after *t* = 120 min and *t* = 2 days. Values are presented as % of *Z* at *t* = 0 min/*t* = 120 min/*t* = 2 days. [c]Values from enzymatic assays. [d]Calculated with B_{max} value for the caudate putamen and from the whole brain from ref 42 and the IC_{50}'s from TrkB. [e]Not tested.

dx.doi.org/10.1021/cn500193f | ACS Chem. Neurosci. 2015, 6, 260−276

Scheme 3. Synthesis and Photoisomerization of (*Z*)-[^{18}F]7b[a]

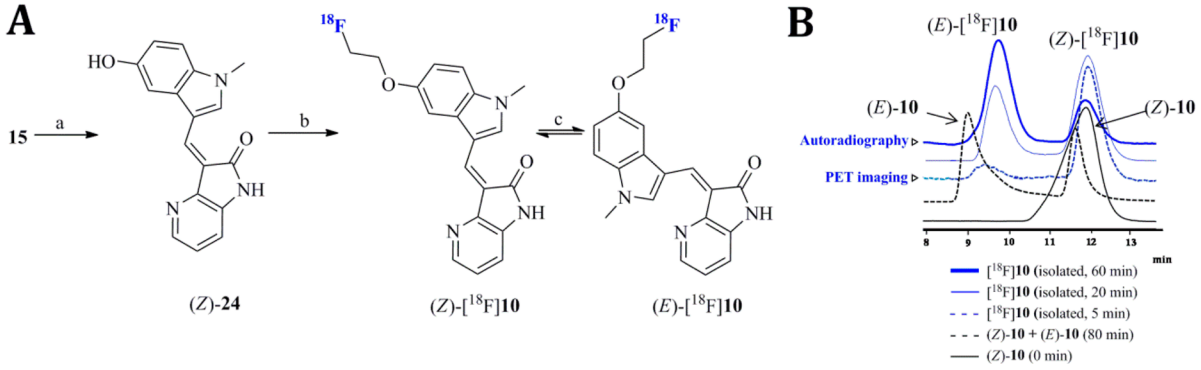

[a](A) Reagents and conditions: (a) **22b**, AcOH, HCl_{conc}, 40 °C, 12 h (44%); (b) KOH(s), [^{18}F]FETos, DMF, 90 °C, 10 min (2.5% ± 0.6% RCY, n = 4, non-decay-corrected isolated yield from $^{18}F^{-}/H_2O$); (c) ambient light. (B) HPLC radiodetection QC of the collected (*Z*)-[^{18}F]**10** (t_R = 12.3 min) peak at 20 and 80 min postisolation showing racemization leading to the formation of (*E*)-[^{18}F]**10** (t_R = 9.8 min) (blue lines) and UV chromatogram of the corresponding (*Z*)-**10** (t_R = 11.5 min) and isomerized sample (*E* isomer, t_R = 9.0 min) (black lines).

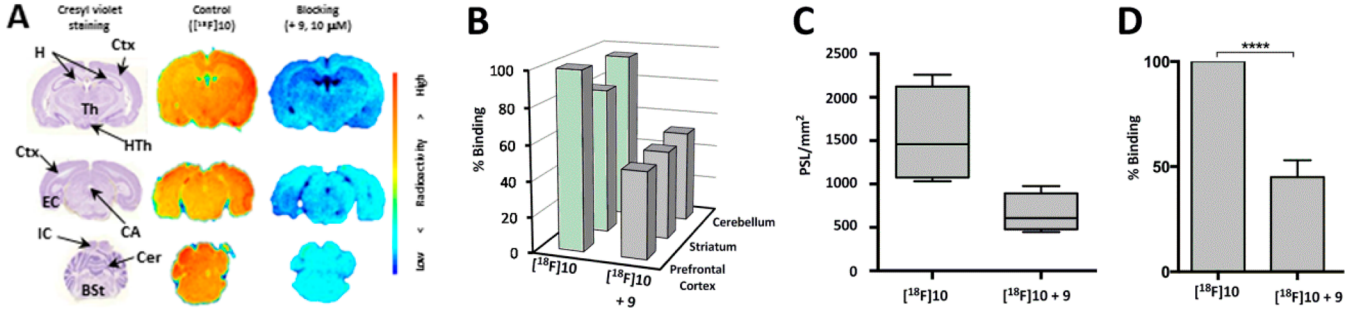

Figure 8. (A) Representative *in vitro* autoradiograms and cresyl violet staining from coronal sections of rat brain showing the binding of [^{18}F]**10** and competition experiments with **9** (10 μM). Autoradiograms have the same absolute intensity range. BSt = brain stem; CA = cerebral aqueduct; Cer = cerebellum; Ctx = cortex; EC = entorhinal cortex; H = hippocampus; HTh = hypothalamus; IC = inferior colliculus; Th = thalamus. (B) Quantitative results of competition experiments for selected regions of interest (ROIs) relative to control for prefrontal cortex. (C, D) Quantitative results of baseline and blocking experiments with neuroblastoma. Human neuroblastoma tumor cryosections (n = 4). PSL/mm^2 = photostimulated luminescence events per square millimeter. Value expressed as mean ± SD (n = 4). ****p < 0.0001.

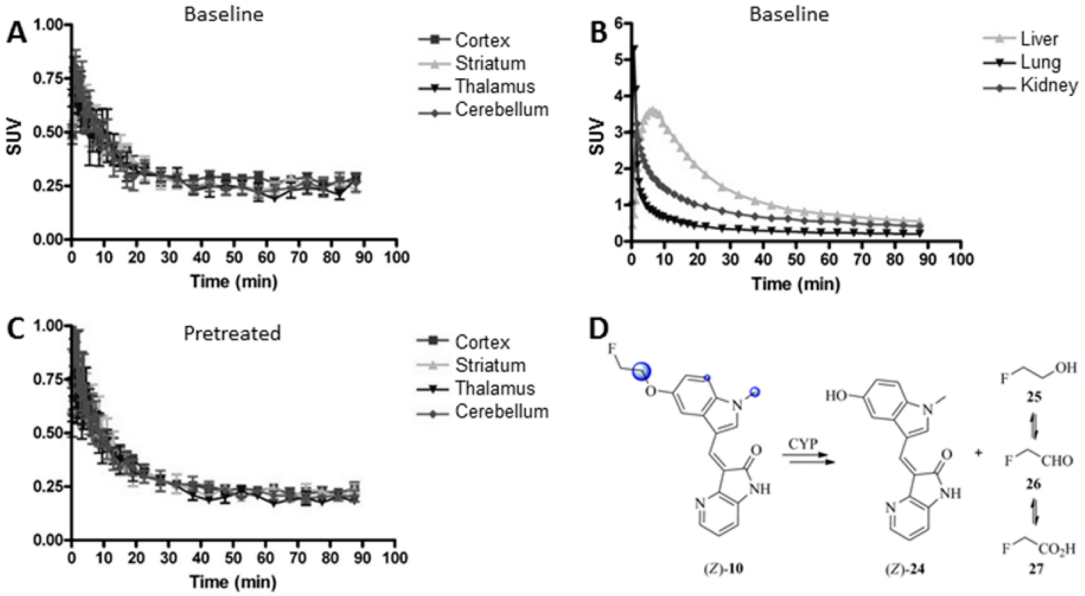

Figure 9. Preliminary metabolism and PET studies with [^{18}F]**10** in Sprague–Dawley in rats. Time–activity curves for (A) brain regions (n = 3) at baseline, (B) selected organs (n = 1), and (C) brain regions (n = 3) for pretreatment studies with **9** (1 mg/kg, iv 15 min prior to [^{18}F]**10** injection, n = 3). SUV, standardized uptake value. (D) *In silico* top predicted CYP-mediated sites of metabolism for (*E*/*Z*)-**10** confirmed by RLM assays.

dx.doi.org/10.1021/cn500193f | ACS Chem. Neurosci. 2015, 6, 260–276

radiosynthesis of [^{18}F]FETos were carried out on a modified PET tracer module (Scintomics GRP) with in-house manifold setup and afforded [^{18}F]FETos in 27.0% ± 2.0% RCY (n = 4, non-decay-corrected isolated yield from $^{18}F^{-}/H_2O$) after reverse-phase HPLC purification. This intermediate was aliquoted and used in a manual procedure for the alkylation of (*Z*)-**24** (typically 0.74 GBq; ∼20 mCi). Following a second HPLC purification, [^{18}F]**10** was obtained in sufficient yields for preliminary biological evaluation (2.5% ± 0.6% ndc RCY, end of bombardment) over a 60 min procedure in >98% radiochemical purity and 122−180 GBq/μmol specific activities. A photoisomerization study of [^{18}F]**10** demonstrated slower isomerization kinetics compared with [^{11}C]**9** (Scheme 3B). Despite the slower rate of photoconversion, the tracer ultimately reached a PSS composed of a ∼2:1 *E*/*Z* mixture when unshielded from light over 60 min, compared with the rapidly reached 1:1 mixture observed for [^{11}C]**9**. The lower rate of isomerization, which turned out to be advantageous in providing the tracer in >90% of the putative potent *Z* isomer for preliminary PET imaging studies (after final formulation, the tracer was immediately injected into the animal to minimize photoconversion), was ascribed to the electron donating nature of the alkyloxy subsitutent in **10**, which may disfavor electron delocalization from the *N*-1′ position of the indole core compared with **9**.

***In Vitro* Autoradiography of [^{18}F]10.** In an analogous study as previously detailed for [^{11}C]**9**, the distribution of [^{18}F]**10** in rat brain and human neuroblastoma was assessed (Figure 8). Binding of [^{18}F]**10** in the rat brain was rather ubiquitous, similar to our previous results with [^{11}C]**9**. Yet, a more detailed analysis of selected regions of interest (prefrontal cortex, striatum, and cerebellum) revealed small regional differences. Binding to the prefrontal cortex and the cerebellum (TrkB/C-rich regions) was more pronounced than what was found for the striatum (TrkA-rich region), which is in line with the Trk isoform selectivity of **10** and the regional concentration of the different Trk receptors. In the presence of an excess of unlabeled **9**, binding of [^{18}F]**10** was significantly reduced in all evaluated regions (Δ = −52% for prefrontal cortex, Δ = −39% for striatum and Δ = −45% for cerebellum, Figure 8A,B). Binding to neuroblastoma cryosections was heterogeneous (Figure 8C) and also significantly reduced by pretreatment with excess **9** (Δ = −55.0% ± 8.0%, n = 4; Figure 8D, see also Figure S12, Supporting Information).

Preliminary *in Vivo* PET Imaging of [^{18}F]10 in Rats. The evaluation of the *in vivo* distribution of [^{18}F]**10** was assessed with PET in rats (tracer at injection was >90% (*Z*)-[^{18}F]**10**, Figure 9A,B). Similar to the results obtained with [^{11}C]**9**, the regional brain distribution of [^{18}F]**10** was uniform. Yet, a major difference regarding phase I metabolism arose when [^{18}F]**10** was compared with [^{11}C]**9**. Whereas the nonfluorinated inhibitor **9** was found to be stable in RLM assays, the fluoroethoxy-linked inhibitor **10** was highly susceptible toward CYP450 metabolism at the 2-fluoroethoxy *C*-1 position. Rapid formation of **24** detected by HPLC was observed. This ultimately led to the formation of more polar metabolites, presumably further desmethylated/hydroxylated products (Figure 9D). Those results were paralleled by *in silico* predictions (O-dealkylation ≫ N-dealkylation > C-hydroxylation). The immediate consequence of this oxidative metabolism for [^{18}F]**10** was the sustained formation of ^{18}F-labeled brain penetrating metabolites stemming from the release and further *in vivo* reduction/oxidation of 2-[^{18}F]fluoroacetaldehyde (**26**, Figure 4D).[61] Moreover, pretreatment with **9** (1 mg/kg, iv, 15 min prior to tracer injection) did not alter brain pharmacokinetics or maximal radioactivity uptake significantly. This is consistent with the brain distribution being dominated by radiometabolites that are inactive toward Trk. This suggests that further structural derivatization is needed to arrive at a fluorinated 3-indolydene 4-aza-2-oxindole scaffold suitable for Trk PET radioligands. For example, a fluoroalkyl chain without phenolic oxygen might be required in order to avoid unwanted elimination of the radionuclide bearing moiety.

■ CONCLUSION

In summary, we have explored the 3-indolydene 4-aza-2-oxindole scaffold for the potential development of pan-Trk PET ligands. We presented the radiosynthesis of 3-(([^{11}C]-1-methyl-1*H*-indol-3-yl)methylene)-1*H*-pyrrolo[3,2-*b*]pyridin-2(3*H*)-one ([^{11}C]GW441756, [^{11}C]**9**) along with the synthesis, photoisomerism characterization, and biological evaluation of the corresponding nonradioactive highly potent inhibitor. Promising *in vitro* and *in vivo* profiles of [^{11}C]**9** led to the radiosynthesis of [^{18}F]**10** selected from a small series of novel highly potent pan-Trk inhibitors. [^{18}F]**10** displayed excellent Trk selectivity in a panel of brain and cancer relevant kinases and Trk-specific binding *in vitro* in rat brain and human neuroblastoma cryosections. PET imaging studies in rodents provided valuable biodistribution information. Radioligand [^{11}C]**9** exhibited higher brain uptake and metabolic stability toward CYP450 compared with [^{18}F]**10**. In both cases, albeit for distinct reasons, the radioactivity in the brain was nonspecifically distributed. Currently, the major drawback of those tracers as a potential class of Trk-targeted PET ligands remains their propensity toward photoisomerization even though we could show that small structural modifications may have a significant impact on the rate of formation and isomer ratios in the PSS (compound **9** vs **10**). Hence, structural optimization is underway to generate an isomerically and metabolically stable counterpart to the 3-indolydene 4-aza-2-oxindole scaffold. Collectively, this work constitutes the first promising basis for future developments of Trk radioligands for *in vivo* PET imaging.

■ METHODS

General. All moisture sensitive reactions were carried out in oven-dried flasks under nitrogen atmosphere with dry solvents. Reagents and solvents were purchased at the highest commercial quality from Fisher, Sigma-Aldrich, or Alfa-Aesar and were used without further purification unless specified otherwise. Organic solutions were concentrated under reduced pressure on a Heidolph rotary evaporator. In general, reactions were magnetically stirred and monitored by TLC performed on precoated glass-backed TLC plates (Analtech, 250 μm) and chromatographic purification of products was accomplished using flash chromatography on Alfa-Aesar silica gel (230−450 mesh). TLC visualization was performed by fluorescence quenching, $KMnO_4$, or ninhydrin. ^{1}H NMR and ^{13}C NMR spectra were recorded on a 300 Varian Mercury spectrometer in $CDCl_3$ or d_6-DMSO and peak positions are given in parts per million using TMS as internal standard. Peaks are reported as s = singlet, d = doublet, t = triplet, q = quartet, p = quintet, m = multiplet, b = broad; coupling constant(s) given in hertz; integration. High resolution mass spectra (HRMS) and LC-MS/MS analysis were obtained from the Regional Center for Mass Spectrometry of The Chemistry Department of the Université de Montréal (LC-MSD-TOF Agilent). Radio TLCs were monitored using Mini Gita (Raytest). [^{11}C]MeI for radiolabeling was prepared by reducing cyclotron-produced [^{11}C]carbon dioxide ([^{11}C]CO_2) (IBA cyclotron (Cyclon 18/9); prepared by the ^{14}N(p,α)^{11}C reaction with

0.5% O_2. Lithium aluminum hydride ($LiAlH_4$) in THF reduced $[^{11}C]CO_2$ to $[^{11}C]$methanolate, followed by iodination with 57% hydroiodic acid. Gamma counting was performed using a CRC-25PET dose calibrator (Capintec, Ramsey, NJ, USA). No-carrier-added (nca) aqueous $[^{18}F]$fluoride was prepared by the $^{18}O(p,n)^{18}F$ nuclear reaction on an enriched $[^{18}O]$water (98%) target.

HPLC Methods. Analytical and radio-preparative HPLC experiments were performed on an Agilent 1200 system (Agilent Technologies, Santa Clara, CA, USA; running on Agilent ChemStation software) equipped with a Raytest Gabi Star radioactivity detector (Raytest Isotopenmessgeräte GmbH, Straubenhardt, Germany) and a Phenomenex aeris peptide 3.6u XB-C18 colomn (250 mm × 4.60 mm). Method A was performed as follows: elution at 0.8 mL min^{-1} with a mixture of H_2O (A) and MeCN (B) isocratic at 40% A and 60% B ($t_{r(Z)\text{-}9}$ = 4.48 min, $t_{r(E)\text{-}9}$ = 5.28 min). Method B was performed as follows: elution at 0.6 mL min^{-1} with a mixture of H_2O (A) and MeCN (B) starting at 80% A from 0 to 1 min, decreasing from 80% A to 50% A from 1 to 3 min, remaining at 50% A from 3 to 20 min ($t_{r(Z)\text{-}9}$ = 15.59 min, $t_{r(E)\text{-}9}$ = 18.49 min). Method C was performed as follows: elution at 0.4 mL min^{-1} with a mixture of H_2O (A) and MeCN (B) starting at 80% A at 0 min and decreasing to 50% A from 0 to 3 min, remaining at 50% A from 3 to 30 min ($t_{r(Z)\text{-}9}$ = 21.24 min, $t_{r(E)\text{-}9}$ = 25.17 min). Method D was performed as follows: elution at 0.4 mL min^{-1} with a mixture of H_2O (A) and MeCN (B) isocratic at 50% A and 50% B ($t_{r(Z)\text{-}9}$ = 7.87 min, $t_{r(E)\text{-}9}$ = 10.17 min). Method Ewas performed as follows: (Phenomenex partisil 5u OSD(3) column (250 mm × 4.60 mm) elution at 1.0 mL min^{-1} with a mixture of H_2O (A) and MeCN (B) isocratic at 30% A and 70% B ($t_{r(Z)\text{-}9}$ = 4.99 min, $t_{r(E)\text{-}9}$ = 5.54 min). Method F was performed as follows: (Phenomenex partisil 5u OSD(3) colomn (250 mm × 4.60 mm) elution at 1.0 mL min^{-1} with a mixture of H_2O (A) and MeCN (B) isocratic at 50% A and 50% B ($t_{r(Z)\text{-}10}$ = 11.5 min, $t_{r(E)\text{-}10}$ = 9.0 min).

Chemical Synthesis. *Diethyl (3-Nitropyridin-2-yl)-malonate (**12**).* To a solution of sodium hydride (60% dispersion in oil, 0.6 g, 25 mmol, 2.3 equiv) in DMSO (25 mL) was added dimethyl malonate (3.8 mL, 25 mmol, 2.3 equiv) dropwise over 20 min, and the mixture was stirred for an additional 30 min at room temperature. 2-Chloro-3-nitropyridine (1.74 g, 11 mmol, 1 equiv) was added to the reaction, and the reaction was heated at 100 °C for 1 h. The reaction was cooled to room temperature and poured into aqueous ammonium chloride (saturated solution, 45 mL). The aqueous solution was extracted with ethyl acetate. The combined organic phases were dried over Na_2SO_4 and concentrated *in vacuo*. The crude residue was purified by flash chromatography (30% EtOAc/hexane), affording 3.0 g of the title compound as a orange oil (97%). R_f 0.40 (30% EtOAc/hexane). ^1H NMR (300 MHz, $CDCl_3$) δ 8.81 (d, J = 4.5 Hz, 1H), 8.48 (d, J = 8.4 Hz, 1H), 7.52 (dd, J = 8.4 Hz, J = 4.8 Hz, 1H), 5.51 (s, 1H), 4.28 (q, J = 7.2 Hz, 4H), 1.27 (t, J = 7.2 Hz, 6H) ppm. ^{13}C NMR (300 MHz, $CDCl_3$) δ 166.4, 153.0, 149.0, 144.8, 133.2, 123.8, 62.1, 59.3, 13.9 ppm. HRMS (APCI) calcd for $C_{12}H_{14}N_2O_6$ $(M + H)^+$ 283.09246, found 283.09175.

*Ethyl 2-(3-Nitro-pyridin-2-yl)-acetate (**13**).* A suspension of diethyl (3-nitropyridin-2-yl)-malonate (5.6 g, 20 mmol, 1 equiv) in DMSO (65 mL) and water (0.37 mL, 20 mmol, 1 equiv) was mixed with lithium chloride (2.1 g, 50 mmol, 2.5 equiv) at room temperature. The reaction was heated to 100 °C overnight, and more lithium chloride (1 g, 24 mmol) was added to the reaction. The reaction was heated for another 6 h and cooled to room temperature. The reaction mixture was poured into brine (100 mL), and the aqueous phase was extracted ethyl acetate. The organic layers were combined, dried over Na_2SO_4, and concentrated *in vacuo*. The crude residue was purified by flash chromatography (10−50% EtOAc/hexane), affording 4.1 g of the title compound as a red oil (98%). R_f 0.62 (50% EtOAc/hexane). ^1H NMR (300 MHz, $CDCl_3$) δ 8.77 (d, J = 4.5 Hz, 1H), 8.41 (d, J = 8.4 Hz, 1H), 7.47 (dd, J = 8.4 Hz, J = 4.5 Hz, 1H), 4.31 (s, 2H), 4.17 (q, J = 7.2 Hz, 2H), 1.24 (t, J = 7.2 Hz, 3H) ppm. ^{13}C NMR (300 MHz, $CDCl_3$) δ 169.1, 153.0, 150.0, 132.9, 123.2, 109.9, 61.4, 43.2, 14.0 ppm. HRMS (APCI) calcd for $C_9H_{11}N_2O_4$ $(M + H)^+$ 211.07133, found 211.07186.

*Ethyl 2-(3-Amino-pyridin-2-yl)-acetate (**14**).* To a solution of ethyl 2-(3-nitro-pyridin-2-yl)-acetate (2.7 g, 13 mmol, 1 equiv) in ethanol (20 mL) was added Pd/C (10%, 0.2 g) slowly. The reaction was placed under an atmosphere of hydrogen and stirred at room temperature for 6 h. The reaction was filtered through Celite, and the filtrate was concentrated *in vacuo* (98%). R_f 0.28 (50% EtOAc/hexane). ^1H NMR (300 MHz, DMSO) δ 7.94 (d, J = 5.4 Hz, 1H), 7.70 (d, J = 8.7 Hz, 1H), 7.59 (dd, J = 8.7 Hz, J = 5.4 Hz, 1H), 6.51 (s, 2H), 4.17 (s, 2H), 4.09 (q, J = 6.9 Hz, 2H), 1.17 (t, J = 6.9 Hz, 3H) ppm. ^{13}C NMR (300 MHz, $CDCl_3$) δ 168.1, 147.2, 131.9, 128.7, 128.0, 126.4, 61.5, 34.1, 14.4 ppm. HRMS (APCI) calcd for $C_9H_{13}N_2O_2$ $(M + H)^+$ 181.09715, found 181.09642.

*1H-Pyrrolo[3,2-b]pyridin-2(3H)-one (4-Aza-2-oxindole) (**15**).* To a solution of ethyl 2-(3-amino-pyridin-2-yl)-acetate (2.4 g, 13 mmol, 1 equiv) in diethyl ether (100 mL) at room temperature was added a hydrochloric acid solution (2 M, 50 mL), and the reaction was stirred for 12 h. The diethyl ether was removed *in vacuo*, and the aqueous phase was brought to pH 7 and concentrated *in vacuo*. The crude residue was purified by flash chromatography (5% MeOH/AcOEt), affording 0.92 g of the title compound as a beige solid (52%). R_f 0.28 (5% MeOH/EtOAc). ^1H NMR (300 MHz, DMSO-d_6) δ 10.50 (s, 1H), 8.03 (dd, J = 4.7 Hz, J = 1.8 Hz, 1H), 7.15−7.08 (m, 2H), 3.55 (s, 2H) ppm. ^{13}C NMR (300 MHz, DMSO-d_6) δ 174.7, 149.0, 141.9, 138.9, 122.8, 115.4 ppm. HRMS (ESI) calcd for $C_7H_7N_2O$ $(M + H)^+$ 135.05529, found 135.05499.

*(3Z)-3-[(1-Methyl-1H-indol-3-yl)methylene]-1,3-dihydro-2H-pyrrolo[3,2-b]pyridin-2-one ((Z)-**9**).* 1-Methylindole-3-carboxaldehyde (0.318 g, 2 mmol, 1 equiv), 4-aza-2-oxindole (0.268 g, 2 mmol, 1 equiv), acetic acid (20 mL), and concentrated HCl (5 mL) were combined at room temperature and then warmed to 40 °C for 12 h. The mixture was concentrated *in vacuo*, and the crude was added to a $NaHCO_3$ solution (sat.) and extracted several times with ethyl acetate. The organic layers were combined, dried over Na_2SO_4, and concentrated *in vacuo*. The crude residue was purified by flash chromatography (5% MeOH/AcOEt), affording 340 mg of a red solid (65%), and was then recrystallized from MeOH/EtOAc. R_f 0.79 (5% MeOH/EtOAc). ^1H NMR (300 MHz, DMSO) δ 10.66 (s, 1H), 9.48 (s, 1H), 8.33 (s, 1H), 8.12 (dd, J = 4.8 Hz, J = 1.5 Hz, 1H), 7.97 (dd, J = 6.6 Hz, J = 1.8 Hz, 1H), 7.60 (dd, J = 6.6 Hz, J = 1.8 Hz, 1H), 7.31 (m, 2H), 7.15 (dd, J = 7.8 Hz, J = 1.5 Hz, 1H), 7.08 (dd, J = 7.8 Hz, J = 4.8 Hz, 1H), 3.95 (s, 3H) ppm. ^{13}C NMR (300 MHz, $CDCl_3$) δ 167.2, 145.4, 141.6, 139.0, 137.2, 134.2, 129.0, 128.9, 123.4, 122.3, 121.7, 118.3, 117.4, 115.2, 111.5, 110.8, 34.1 ppm. HRMS (ESI) calcd for $C_7H_7N_2O$ $(M + H)^+$ 276.11314, found 276.11266.

*(3E)-3-[(1H-Indol-3-yl)methylene]-1,3-dihydro-2H-pyrrolo[3,2-b]-pyridin-2-one (**16**).* Indole-3-carboxaldehyde (0.318 g, 2 mmol, 1 equiv), 4-aza-2-oxindole (0.268 g, 2 mmol, 1 equiv), acetic acid (20 mL), and concentrated HCl (5 mL) were combined at room temperature and then warmed to 40 °C for 12 h. The mixture was concentrated *in vacuo*, and the crude was added to a $NaHCO_3$ solution (sat.) and extracted several times with ethyl acetate. The organic layers were combined, dried over Na_2SO_4, and concentrated *in vacuo*. The crude residue was purified by flash chromatography (100% AcOEt), affording 350 mg of a yellow solid (75%). R_f 0.66 (100% EtOAc). ^1H NMR (300 MHz, DMSO) δ 12.26 (s, 1H), 10.53 (s, 1H), 10.02 (s, 1H), 8.28 (d, J = 4,17 Hz, 1H), 8.06 (s, 1H), 7.92 (m, 1H), 7.55 (m, 1H), 7.26−7.13 (m, 4H) ppm. ^{13}C NMR (300 MHz, $CDCl_3$) δ 168.9, 144.1, 141.5, 136.9, 136.8, 136.6, 130.5, 128.4, 123.3, 121.9, 118.3, 117.7, 115.4, 113.1, 112.2, 109.9 ppm. HRMS (ESI) calcd for $C_7H_7N_2O$ $(M + H)^+$ 262.09749, found 262.09742.

*(Z)-3-((5-(2-Fluoroethoxy)-1-methyl-1H-indol-3-yl)methylene)-1,3-dihydro-2Hpyrrolo[3,2-b]pyridine-2-one ((Z)-**10**).* The general procedure used for the synthesis of (*Z*)-**9** was followed using 5-(2-fluoroethoxy)-1-methyl-1*H*-indole-3-carbaldehyde (0.123 g, 0.55 mmol) as starting material. The crude residue was purified by flash chromatography (100% AcOEt), affording 81.0 mg of a red solid (43%). R_f 0.42 (80% EtOAc/hexane). ^1H NMR (300 MHz, DMSO-d_6) δ 10.64 (s, 1H), 9.45 (s, 1H), 8.33 (s, 1H), 8.11 (dd, J = 4.8 Hz, J = 1.5 Hz, 1H), 7.52 (s, 1H), 7.51 (d, J = 6.3 Hz, 1H), 7.14 (dd, J = 7.8 Hz, J = 1.5 Hz, 1H), 7.08 (dd, J = 7.65 Hz, J = 4.8 Hz, 1H), 6.96 (dd, J

= 8.85 Hz, J = 2.4 Hz, 1H), 4.77 (td, J = 47.7 Hz, J = 3.9 Hz, 2H), 4.37 (td, J = 30.6 Hz, J = 3.9 Hz, 2H), 3.92 (s, 3H) ppm. ^{13}C NMR (75 MHz, DMSO-d_6) δ 167.3, 155.0, 145.6, 141.5, 139.3, 134.1, 132.4, 129.9, 129.4, 121.5, 116.7, 115.1, 113.8, 112.5, 110.9, 101.3, 82.0 (J = 165.6 Hz), 67.7 (J = 18.9 Hz), 34.2 ppm. HRMS (ESI) calcd for $C_{19}H_{17}FN_3O_2$ (M + H)$^+$ 338.12993, found 338.13073.

*(Z)-3-((6-(2-Fluoroethoxy)-1-methyl-1H-indol-3-yl)methylene)-1,3-dihydro-2Hpyrrolo[3,2-b]pyridine-2-one ((Z)-**18a**).* The general procedure used for the synthesis of (*Z*)-**9** was followed using 6-(2-fluoroethoxy)-1-methyl-1*H*-indole-3-carbaldehyde (0.133 g, 0.6 mmol) as starting material. The crude residue was purified by flash chromatography (100% AcOEt), affording 106.5 mg of a red solid (53%). R_f 0.42 (80% EtOAc/hexane). ^{1}H NMR (300 MHz, DMSO-d_6) δ 10.64 (s, 1H), 9.37 (s, 1H), 8.27 (s, 1H), 8.11 (d, J = 4.8 Hz, 1H), 7.85 (d, J = 8.7 Hz, 1H), 7.21 (d, J = 1.2 Hz, 1H), 7.16−7.06 (m, 2H), 6.95 (dd, J = 8.7 Hz, J = 1.8 Hz, 1H), 4.77 (td, J = 48 Hz, J = 3.3 Hz, 2H), 4.37 (td, J = 30.3 Hz, J = 3.6 Hz, 2H), 3.90 (s, 3H) ppm. ^{13}C NMR (75 MHz, DMSO-d_6) δ 167.1, 156.0, 145.4, 141.6, 138.4, 138.1, 134.2, 129.0, 123.1, 121.6, 119.2, 117.4, 115.2, 112.1, 110.9, 96.2, 82.0 (J = 165.6 Hz), 68.0 (J = 18.9 Hz), 34.1 ppm. HRMS (ESI) calcd for $C_{19}H_{17}FN_3O_2$ (M + H)$^+$ 338.12993, found 338.13069.

*(E)-3-((4-Methoxy-1H-indol-3-yl)methylene)-1,3-dihydro-2H-pyrrolo[3,2-b]pyridine-2-one ((E)-**18b**).* The general procedure used for the synthesis of (*Z*)-**9** was followed using 4-methoxy-1*H*-indole-3-carboxaldehyde (0.100 g, 0.57 mmol) as starting material. The crude residue was purified by flash chromatography (100% AcOEt), affording 120.0 mg of a red solid (72%). R_f 0.48 (80% EtOAc/hexane). ^{1}H NMR (300 MHz, DMSO-d_6) δ 12.21 (s, 1H), 10.50 (s, 1H), 10.09 (s, 1H), 8.68 (s, 1H), 8.26 (d, J = 4.8 Hz, 1H), 7.20−7.11 (m, 4H), 6.77 (d, J = 6.9 Hz, 1H), 3.97 (s, 3H) ppm. ^{13}C NMR (75 MHz, DMSO-d_6) δ 169.0, 154.9, 144.1, 141.2, 138.4, 136.7, 136.2, 134.9, 124.2, 121.7, 117.3, 116.8, 115.2, 113.2, 106.2, 103.0, 55.8 ppm. HRMS (ESI) calcd for $C_{17}H_{14}N_3O_2$ (M + H)$^+$ 292.10805, found 292.10858.

*(Z)-3-((5-Methoxy-1-methyl-1H-indol-3-yl)methylene)-1,3-dihydro-2H-pyrrolo[3,2-b]pyridine-2-one ((Z)-**18c**).* The general procedure used for the synthesis of (*Z*)-**9** was followed using 5-methoxy-1-methyl-1*H*-indole-3-carbaldehyde (0.151 g, 0.8 mmol) as starting material. The crude residue was purified by flash chromatography (3% MeOH/DCM), affording 149.7 mg of a red solid (61%). R_f 0.25 (3% MeOH/DCM). ^{1}H NMR (300 MHz, DMSO-d_6) δ 10.63 (s, 1H), 9.44 (s, 1H), 8.32 (s, 1H), 8.11 (d, J = 4.5 Hz, 1H), 7.50 (d, J = 9 Hz, 1H), 7.45 (d, J = 2.4 Hz, 1H), 7.15−7.06 (m, 2 H), 6.92 (dd, J = 8.7 Hz, J = 2.1 Hz, 1H), 3.91 (s, 3H), 3.87 (s, 3H) ppm. ^{13}C NMR (75 MHz, DMSO-d_6) δ 167.3, 156.2, 145.6, 141.5, 139.3, 134.0, 132.2, 129.9, 129.4, 121.4, 116.6, 115.1, 113.3, 112.4, 110.8, 100.3, 55.9, 34.2 ppm. HRMS (ESI) calcd for $C_{18}H_{16}N_3O_2$ (M + H)$^+$ 306.1237, found 306.12434.

*(Z)-3-((1-(2-Fluoroethyl)-1H-indol-3-yl)methylene)-1,3-dihydro-2H-pyrrolo[3,2-b]pyridin-2-one ((Z)-**18d**).* The general procedure used for the synthesis of (*Z*)-**9** was followed using 1-(2-fluoroethyl)-1*H*-indole-3-carbaldehyde (0.153 g, 0.55 mmol) as starting material. The crude residue was purified by flash chromatography (4% MeOH/DCM), affording 159.0 mg of a red solid (64%). R_f 0.46 (4% MeOH/DCM). ^{1}H NMR (300 MHz, DMSO-d_6) δ 10.67 (s, 1H), 9.56 (s, 1H), 8.34 (s, 1H), 8.13 (dd, J = 4.5 Hz, J = 0.6 Hz, 1H), 8.00−7.97 (m, 1H), 7.71−7.67 (m, 1H), 7.35−7.27 (m, 2H), 7.18−7.09 (m, 2H), 4.82 (td, J = 39.6 Hz, J = 4.2 Hz, 2H), 4.69 (td, J = 20.7 Hz, J = 4.5 Hz, 2H) ppm. ^{13}C NMR (75 MHz, DMSO-d_6) δ 167.2, 145.3, 141.7, 138.4, 136.6, 134.4, 129.0, 128.7, 123.5, 122.4, 121.9, 118.4, 118.1, 115.3, 111.7, 111.2, 82.0 (J = 167.2 Hz), 47.5 (J = 19.6 Hz) ppm. HRMS (ESI) calcd for $C_{18}H_{15}FN_3O$ (M + H)$^+$ 308.11937, found 308.12011.

*(Z)-3-((6-Methoxy-1-methyl-1H-indol-3-yl)methylene)-1,3-dihydro-2H-pyrrolo[3,2-b]pyridine-2-one ((Z)-**18e**).* The general procedure used for the synthesis of (*Z*)-**9** was followed using 6-methoxy-1-methyl-1*H*-indole-3-carbaldehyde (0.100 g, 0.53 mmol) as starting material. The crude residue was purified by flash chromatography (3% MeOH/DCM), affording 97.0 mg of a red solid (60%). R_f 0.37 (3% MeOH/DCM). ^{1}H NMR (300 MHz, DMSO-d_6) δ 10.64 (s, 1H), 9.36 (s, 1H), 8.26 (s, 1H), 8.11 (dd, J = 4.5 Hz, J = 1.0 Hz, 1H), 8.83 (d, J = 8.7 Hz, 1H), 7.15−7.06 (m, 3H), 6.91 (dd, J = 8.7 Hz, J = 1.8 Hz, 1H), 3.91 (s, 3H), 3.83 (s, 3H) ppm. ^{13}C NMR (75 MHz, DMSO-d_6) δ 167.1, 157.3, 145.5, 141.6, 138.2, 138.1, 134.1, 129.1, 122.8, 121.6, 119.1, 117.3, 115.2, 111.9, 110.9, 95.1, 55.9, 34.1 ppm. HRMS (ESI) calcd for $C_{18}H_{16}N_3O_2$ (M + H)$^+$ 306.1237, found 306.12424.

*(Z)-3-((5-Hydroxy-1-methyl-1H-indol-3-yl)methylene)-1,3-dihydro-2H-pyrrolo[3,2-b]pyridine-2-one ((Z)-**24**).* The general procedure used for the synthesis of (*Z*)-**9** was followed using 5-hydroxy-1-methyl-1*H*-indole-3-carbaldehyde (0.125 g, 0.72 mmol) as starting material. The crude residue was purified by flash chromatography (5% MeOH/DCM), affording 92.0 mg of a red solid (44%). R_f 0.41 (5% MeOH/DCM). ^{1}H NMR (300 MHz, DMSO-d_6) δ 10.61 (s, 1H), 9.36 (s, 1H), 9.26 (s, 1H), 8.18 (s, 1H), 8.10 (dd, J = 4.8 Hz, J = 1.2 Hz, 1H), 7.41 (d, J = 8.7 Hz, 1H), 7.20 (d, J = 2.1 Hz, 1 H), 6.92 (dd, J = 8.7 Hz, J = 2.1 Hz, 1H), 7,15−7.04 (m, 3H), 6.81 (dd, J = 8.7 Hz, J = 1.8 Hz, 1H), 3.89 (s, 3H) ppm. ^{13}C NMR (75 MHz, DMSO-d_6) δ 167.3, 153.9, 145.6, 141.6, 139.1, 133.9, 131.6, 130.3, 129.0, 121.3, 116.1, 115.1, 113.2, 112.3, 110.3, 102.4, 34.2 ppm. HRMS (ESI) calcd for $C_{17}H_{14}N_3O_2$ (M + H)$^+$ 292.10805, found 292.10861.

*1-(2-Fluoroethyl)-1H-indole-3-carbaldehyde (**20**).* To a solution of 1*H*-indole-3-carbaldehyde (300 mg, 2.07 mmol, 1 equiv) in THF (5 mL) was added sodium hydride (60% dispersion in oil, 83 mg, 2.07 mmol, 1 equiv), and the mixture was stirred at 0 °C during 10 min. 2-Fluoroethyl 4-methylbenzenesulfonate (904 mg, 4.14 mmol, 2 equiv) was added dropwise, and the reaction mixture was warmed at room temperature for 12 h. Water was added, and the aqueous layer was extracted with ethyl acetate 3 times. The combined organics layers were dried with Na_2SO_4 and concentrated *in vacuo*. The crude residue was purified by flash chromatography (0−3% MeOH/DCM), affording 379 mg of an orange solid (96%). R_f 0.80 (3% MeOH/DCM). ^{1}H NMR (300 MHz, $CDCl_3$) δ 10.00 (s, 1H), 8.32 (m, 1H),7.76 (s, 1H), 7.34−7.32 (m, 3H), 4.76 (td, J = 46.8 Hz, J = 4.5 Hz, 2H), 4.45 (td, J = 26.4 Hz, J = 4.8 Hz, 2H) ppm. ^{13}C NMR (75 MHz, $CDCl_3$) δ 184.6, 138.7, 137.0, 125.3, 124.2, 123.0, 122.3, 118.7, 109.6, 81.0 (J = 172.05 Hz), 47.2 (J = 21 Hz) ppm. HRMS (ESI) calcd for $C_{11}H_{11}FNO$ (M + H)$^+$ 192.08192, found 192.08208.

*5-Hydroxy-1-methyl-1H-indole-3-carbaldehyde (**22b**).* To a solution of 5-methoxy-1-methyl-1*H*-indole-3-carbaldehyde (1.0 g, 5.29 mmol, 1 equiv) in DCM (30 mL) was added BBr_3 (1 M in DCM, 26.4 mL, 26.42 mmol, 5 equiv) at 0 °C with stirring for 10 min. The reaction mixture was slowly warmed to room temperature and stirred during 3 h. The temperature was then lowered to 0 °C, MeOH (100 mL) was slowly added, and the pH of the mixture was adjusted to 8 by adding saturated solution of $NaHCO_3$. The organic solvents were removed under reduced pressure, and the remaining aqueous mixture was extracted with ethyl acetate 5 times. The organic layers were combined, dried over Na_2SO_4, filtered, and evaporated under reduced pressure. To the crude residue was added DCM, and the precipitate was filtered off. The solid was air-dried to give the title compound as 870 mg of purple powder (94%). R_f 0.28 (5% MeOH/DCM). ^{1}H NMR (300 MHz, DMSO-d_6) δ 9.77 (s, 1H), 9.10 (s, 1H), 8.06 (s, 1H), 7.48 (d, J = 2.4 Hz, 1H), 7.31 (d, J = 8.7 Hz, 1H), 6.77 (dd, J = 8.7 Hz, J = 2.4 Hz, 1H), 3.79 (s, 3H) ppm. ^{13}C NMR (300 MHz, DMSO-d_6) δ 184.2, 154.1, 141.5, 132.4, 126.1, 116.8, 113.5, 111.7, 105.9, 33.8 ppm. HRMS (ESI) calcd for $C_{10}H_{10}NO_2$ (M + H)$^+$ 176.0706, found 176.07042.

*6-Hydroxy-1-methyl-1H-indole-3-carbaldehyde (**22a**).* The general procedure used for the synthesis of 5-hydroxy-1-methyl-1*H*-indole-3-carbaldehyde was followed using 6-methoxy-1-methyl-1*H*-indole-3-carbaldehyde (200 mg, 1.06 mmol) as starting material (quantitative). R_f 0.54 (5% MeOH/DCM). ^{1}H NMR (300 MHz, DMSO-d_6) δ 9.76 (s, 1H), 9.40 (s, 1H), 8.03 (s, 1H), 7.84 (d, J = 8.7 Hz, 1H), 7.03 (d, J = 1.2 Hz, 1H), 6.75 (dd, J = 8.7 Hz, J = 1.2 Hz, 1H), 3.75 (s, 3H) ppm. ^{13}C NMR (300 MHz, DMSO-d_6) δ 184.3, 155.2, 141.0, 139.5, 122.0, 117.8, 117.6, 112.8, 96.5, 33.6 ppm. HRMS (ESI) calcd for $C_{10}H_{10}NO_2$ (M + H)$^+$ 176.0706, found 176.06982.

*5-(2-Fluoroethoxy)-1-methyl-1H-indole-3-carbaldehyde (**23b**).* To a solution of 5-hydroxy-1-methyl-1*H*-indole-3-carbaldehyde (195.5 mg, 1.12 mmol, 1 equiv) in DMF (15 mL) was added

potassium carbonate (308 mg, 2.23 mmol, 2 equiv). The reaction mixture was stirred at room temperature during 10 min. 2-Fluoroethyl 4-methylbenzenesulfonate (489 mg, 2.24 mmol, 2 equiv) was added dropwise, and the reaction mixture was warmed at 70 °C for 12 h. Water was added after the reaction was cooled to room temperature, and the aqueous layer was extracted with ethyl acetate 3 times. The combined organics layers were dried with Na_2SO_4 and concentrated *in vacuo*. The crude residue was purified by flash chromatography (0−5% MeOH/DCM), affording 169 mg of a yellow solid (72%). R_f 0.55 (80% EtOAc/hexane). ^{1}H NMR (300 MHz, $CDCl_3$) δ 9.91 (s, 1H), 7.77 (d, J = 2.4 Hz, 1H), 7.61 (s, 1H), 7.24 (d, J = 8.4 Hz, 1H), 7.02 (dd, J = 8.4 Hz, J = 2.4 Hz, 1H), 4.78 (td, J = 47.4 Hz, J = 4.2 Hz, 2H), 4.30 (td, J = 28.5 Hz, J = 4.2 Hz, 2H), 3.82 (s, 3H) ppm. ^{13}C NMR (75 MHz, $CDCl_3$) δ 184.3, 155.4, 139.4, 135.8, 133.0, 125.8, 115.0, 110.8, 104.3, 82.0 (J = 169.3 Hz), 67.7 (J = 20.0 Hz), 33.8 ppm. HRMS (ESI) calcd for $C_{12}H_{13}FNO_2$ $(M + H)^+$ 222.09248, found 222.09156.

*6-(2-Fluoroethoxy)-1-methyl-1H-indole-3-carbaldehyde (**23a**).* The general procedure used for the synthesis of 5-(2-fluoroethoxy)-1-methyl-1*H*-indole-3-carbaldehyde was followed using 6-hydroxy-1-methyl-1*H*-indole-3-carbaldehyde (185.0 mg, 1.05 mmol) as starting material, affording 169 mg of a yellow solid (80%). R_f 0.63 (3% MeOH/DCM). ^{1}H NMR (300 MHz, $CDCl_3$) δ 9.88 (s, 1H), 8.15 (d, J = 8.7 Hz, 1H), 7.53 (s, 1H), 6.96 (dd, J = 8.7 Hz, J = 2.1 Hz, 1H), 6.79 (d, J = 2.1 Hz, 1H), 4.77 (td, J = 47.4 Hz, J = 3.9 Hz, 2H), 4.30 (td, J = 27.9 Hz, J = 4.2 Hz, 2H), 3.75 (s, 3H) ppm. ^{13}C NMR (75 MHz, $CDCl_3$) δ 184.2, 156.3, 139.0, 138.7, 122.8, 119.6, 118.1, 112.2, 95.1, 82.0 (J = 169.6 Hz), 67.7 (J = 20.2 Hz), 33.6 ppm. HRMS (ESI) calcd for $C_{12}H_{13}FNO_2$ $(M + H)^+$ 222.09248, found 222.09264.

[γ-^{33}P]ATP-Based Enzymatic Assay. Compound MeOH·(*Z*)-**9** was tested in a [γ-^{33}P]ATP-based enzymatic assay by Reaction Biology Corporation (Malvern, PA). Briefly, the compound was tested in a 10-concentration IC_{50} curve with 3-fold serial dilution starting at 10 μM. The reactions were performed with 1 μM ATP and profiled against three tyrosine kinases (tropomyosin receptor kinase A (TrkA), tropomyosin receptor kinase B (TrkB), and tropomyosin receptor kinase C (TrkC). IC_{50} values less than 5.08×10^{-10} M or higher than 1.00×10^{-5} are estimated based on the best curve fitting available (n = 2). The same procedure was followed for the evaluation of inhibitors **16**, **10**, and **18a−e** (n = 1). Compound **10** was tested for inhibitory activity at 500 nM on a panel of 18 selected kinases (SYK, PDK1/PDHK1, PDGFRa, P38a/MAPK14, KDR/VEGFR2, JNK1, JAK1, ITK, FMS, ERK1, ERBB2/HER2, EGFR, c-SRC, c-MET, c-KIT, BRAF, ALK, and ABL1) under similar conditions (n = 2).

Docking Simulation and Computational Prediction of Sites of Metabolism. Molecular docking simulations of (*Z*)-**9**, (*E*)-**9**, (*Z*)-**10**, and (*E*)-**10** were performed using the X-ray cocrystal structure of TrkB−cpdn5 complex (PDB code 4AT3), TrkA−AZ-23 complex (PDB code 4AOJ), and TrkC−GNF-5837 (PDB code 3V5Q) using the FITTED 3.5 program (FORECASTER platform).[46] Docking structures and figures were prepared using Discovery Studio 3.5 Visualizer. The simulations for the SoM were performed using IMPACTS (FORECASTER platform), which predicts the top two SoM combining docking to metabolic enzymes, transition state modeling, and rule-based substrate reactivity prediction.[50] PDB IDs for enzymes were as follows: CYP1A2, 2HI4; CYP2C9, 1R9O, 1OG2, and 1OG5; CYP2D6, 3QM4; CYP3A4, 1TQN, 1W0E, 1W0F, 1W0G, 2J0D, 2V0M, and 3NXU; CYP2C19, 4GQS.

Radiosynthesis of (*E*/*Z*)-[^{11}C]9. Precursor (*E*)-**15** (1.0 mg, 4 μmol) was placed in a 4.0 mL conical vial containing KOH (half a pellet crushed) and dissolved in acetone (250 μL). [^{11}C]MeI (~0.37 Gbq (10 mCi) for reaction optimization and ~7.4 Gbq (200 mCi) for isolation) was transported by a stream of nitrogen into the reaction vial for 5 min, and the reaction mixture was purified by analytical HPLC using either HPLC method B or HPLC method C (0.037−0.37 GBq (1−10 mCi) HPLC injections). Eluates were monitored for radioactivity and for UV absorbance at 280 nm, and the peak corresponding to (*E*)-[^{11}C]**9** was collected (25.9% ± 5.7% (n = 8) RCY ndc (based on trapped [^{11}C]CH_3I), 29.6−59.2 GBq/μmol (0.8−1.6 Ci/μmol)). When used for PET animal studies, the collected [^{11}C]**9** (isomerized upon light exposure from (*E*)-[^{11}C]**9** peak collection yielding a 1:1 *E*/*Z* mixture) was passed through a preconditioned (10 mL of EtOH followed by 10 mL of water) Sep-Pak C18 Light cartridge, eluted with 0.5−1.0 mL of EtOH, and diluted with sterile saline prior to injection.

Radiosynthesis of (*E*/*Z*)-[^{18}F]10. The azeotropic drying of $^{18}F^-$ and the radiosynthesis of [^{18}F]-FETos[60] were carried out using a modified PET tracer radiosynthesis module (Scintomics GRP, Germany) with a homemade manifold setup operated with Scintomics software. The module was equipped with a radioactivity detector and a Knauer UV detector.

Reaction of [^{18}F]Fluoride with Ethylene Di(p-toluenesulfonate). The $[^{18}F]F^-/H_2O^-$ (~11.1−18.5 GBq, 300−500 mCi) was passed through a Sep-Pak Light QMA cartridge (Waters) as an aqueous solution in ^{18}O-enriched water, and the ^{18}F activity was eluted with 1.0 mL of a Kryptofix 222/K_2CO_3 solution (Kryptofix2.2.2, 10−12 mg, dissolved in 150 μL of 0.125 M K_2CO_3 + 1.3 mL of MeCN) in a 5.0 mL conical vial with a stirring bar. The solvent was removed at 100 °C under reduced pressure, agitation, and a stream of argon gas. The residue was azeotropically dried with 0.5 mL of anhydrous acetonitrile twice at 100 °C. Following azeotropic drying, the reaction vial was charged with ethylene di(*p*-toluenesulfonate) (8−10 mg in 1.0 mL of MeCN), and the mixture was allowed to react for 10 min at 90 °C. The crude [^{18}F]FETos was then diluted with HPLC eluent (1.5 mL, 40% MeCN, 60% H_2O) and injected on HPLC. Preparative radio-HPLC for the isolation of [^{18}F]FETos was performed using a Waters uBondapak C18 10 μm, 125A column (7.8 mm × 300 mm) with an isocratic eluent (40% MeCN/60% H_2O) at 4.0 mL min^{-1}. The [^{18}F]FETos labeling precursor was obtained in 27.0% ± 2.0% RCY, n = 4, non-decay-corrected isolated yield from $^{18}F^-/H_2O$. An aliquot of the product fraction corresponding to [^{18}F]FETos (~1.85 GBq, 50 mCi) was collected and diluted with 50 mL of H_2O and passed through a preconditioned (10 mL of EtOH followed by 10 mL of water) Sep-Pak C18 Plus cartridge and then eluted with 0.5−1.0 mL of DMF, aliquoted, and directly used in the second step.

*Radiosynthesis of (E/Z)-[^{18}F]**10**.* The radiosynthesis of (*Z*)-[^{18}F]**10** using [^{18}F]FETos ([^{18}F]) was carried out manually. [^{18}F]FETos from the previous step (~0.74 GBq, 20 mCi, in 300 μL of DMF) was directly transferred to a 4.0 mL reaction conical vial containing precursor (*Z*)-**24** (1.0 mg, 3.4 μmol) and KOH (half a pellet crushed). The conical vial was sealed and allowed to react at 90 °C for 10 min. The reaction mixture was subsequently quenched with HPLC mobile phase (1 mL, 50% MeCN, 50% H_2O) and cooled at room temperature in an ice bath (2 min). An aliquot of the reaction mixture (~0.2−0.3 GBq, 6−8 mCi) was purified by analytical reverse-phase HPLC, HPLC method F. The eluates were monitored for radioactivity and for UV absorbance (280 nm), and the peak corresponding to (*Z*)-[^{18}F]**10** (~0.74 GBq, 2 mCi) was collected. When used for autoradiography, animal PET, and photoisomerization studies, the collected (*Z*)-[^{18}F]**10** was passed through a preconditioned (10 mL of EtOH followed by 10 mL of water) Sep-Pak C18 Light cartridge, eluted with 0.5−1.0 mL of EtOH, and diluted with sterile saline. The tracer was obtained in 2.5% ± 0.6% RCY (n = 4, non-decay-corrected isolated yield from $^{18}F^-/H_2O$) and >98% radiochemical purity with SA in the range of 122.0−181.3 GBq/μmol (3.3−4.9 Ci/μmol) at the end of synthesis (60−70 min from end of bombardment). The ethanolic solution containing (*E*/*Z*)-[^{18}F]**10** was used for the photoisomerization studies of the tracer with method F. The photoisomerization was previously evaluated for the nonradioactive compound **10** ($t_{r(Z)\text{-}10}$ = 11.5 min, $t_{r(E)\text{-}10}$ = 9.0 min) with 0.7 min calibrated delay between the UV and radiodetector. The determination of SA was achieved by the comparison of the 280 nm UV absorbance peak (integration) of the carrier product with standard calibration curves of the corresponding nonradioactive standards. The peak corresponding to (*Z*)-**10** from nonisomerized solutions kept in light-protected conical vials was used to obtain the calibration curve. Radiochemical purity was determined by HPLC injection of samples from the final ethanolic solutions as the sum of the *E*- and *Z*-isomers.

In Vitro Metabolism of [^{11}C]9 and Nonradioactive 9 and 10. *Plasma Stability.* Compound [^{11}C]**9** (radiochemical purity >99%)

was incubated in rat plasma (500 μL) at 37 °C, and ice-cold acetonitrile (250 μL, after 5, 10, 30, and 60 min) was added for protein precipitation at different time points followed by centrifugation. The amount of intact [^{11}C]**9** was determined by HPLC analysis of the supernatant.

Rat Liver Microsomal Assay. In a shaking water bath at 37 °C, **9** (or **10**, 10.0 μM) was incubated in a final volume of 500 μL of 100 mM phosphate buffer (pH = 7.4) containing pooled rat microsomes (RLM) (0.25 mg/mL protein) together with NADPH regenerating system (solution A, 1.3 mM $NADP^+$, 3.3 mM glucose-6-phosphate, 3.3 mM $MgCl_2$; solution B, 0.4 U/mL glucose-6-phosphate dehydrogenase). Reactions were initiated by successive addition of microsomes in a preincubated mixture (5 min) of NADPH regenerating system and **9**. Aliquots (50 μL) of incubation samples were protein precipitated at 0, 5, 15, 60, and 90 min with 150 μL of ice-cold acetonitrile and centrifuged. The supernatants were analyzed by HPLC. Two control experiments were carried out: first incubation without the NADPH regenerating system (no enzymatic activity) and second incubation without the test compound (baseline).

Computational Physicochemical Properties. CLogP, cLogD (at pH = 7.4), and TPSA values were computed with the program Pallas 3.0 for Windows (CompuDrug; San Francisco, CA).

Western Blot Analysis. Neuroblastoma tissue samples were homogenized in ice-cold RIPA buffer (Tris 50 mM, Nacl 150 mM, SDS 0.1%, sodium deoxycholate 0.5%, Triton X 100 0.1%, 1 mM PMSF, Roche Complete Protease inhibitor tablet), disrupted mechanically, and centrifuged. Protein concentrations of each sample were determined by Bradford method. Next, 10 μg of samples was then separated by SDS-PAGE electrophoresis in Tris-glycine buffer under denaturing conditions and transferred to nitrocellulose membrane (Bio-Rad, Hercules, CA, USA) in Tris-glycine buffer (25 mM Tris, 250 mM glycine, 0.1% SDS; pH 8.3) with 20% methanol. Membranes were blocked with either 2% BSA for phospho-TrkB (TrkBY515; Abcam, Cambridge, MA, USA; ab51187, 1:100) or 5% nonfat milk for TrkB (the polyclonal antibody against TrkB (RTB) has been previously described)[55] in Tris-buffered saline-Tween 20 (TBS-Tween; 25 mM Tris base, 125 mM NaCl, 0.1% Tween 20) for 1 h at room temperature. Membranes were then incubated overnight at 4 °C in 2% BSA or 5% nonfat milk in Tris-buffered saline with primary antibodies. Membranes were rinsed three times for 10 min with TBS-Tween then incubated for 1 h at room temperature with a horseradish peroxidase-conjugated secondary antibody against the primary antibody host species (anti-rabbit from Sigma, St Louis, MO, USA). The membranes were washed three times for 10 min in TBS-Tween. Proteins were detected by enhanced chemiluminescence (ECL reagents; Amersham, Little Chalfont, UK). Monoclonal anti-actin (Fischer, 1:2000) was used as a loading control of each sample.

Autoradiography. Three rats were decapitated; their brains were rapidly removed, frozen in 2-methylbutane (−40 °C), and stored at −80 °C. Brain sections (20 μm thick) were thaw mounted onto Superfrost Plus slides (Thermo Scientific) and stored at −80 °C. Cryogenized human neuroblastoma tumors (Dr. Hervé Sartelet from Sainte-Justine Hospital courteously provided human neuroblastoma samples) were also mounted onto Superfrost Plus slides (Thermo Scientific) and stored at −80 °C. After a preincubation in PBS buffer (30 mmol/L, pH 7.4, containing 137 mmol/L NaCl, 27 mmol/L) for 10 min at room temperature, rat and tumor sections were incubated 60 min (room temperature) in buffer containing [^{11}C]**9** (344 μCi in 1050 mL of buffer total) and 3 h (room temperature) for [^{18}F]**10** (518 μCi in 750 mL buffer total). Compound **9** (10 μM) was used to determine the specific binding of [^{11}C]**9** and [^{18}F]**10**. After three washes in incubation buffer (5 min, 4 °C) and a rapid rinse with ice-cold water (15 s), the sections were dried in a stream of air (room temperature). Sections were then dried further in a vacuum container with formaldehyde powder for mild fixation. Specific binding was calculated as the difference of total and nonspecific binding. Labeled sections were placed on phosphor-imaging plates (BAS 2025; Fuji, Japan), with industrial tritium activity standards (Amersham Biosciences, Piscataway, NJ, USA). On exposure, the plates were scanned with a plate reader (spatial resolution of 50 μm; BAS 5000; Fuji). A correction factor of 3 was applied for the specific binding of the (*Z*)-[^{18}F]**10** isomer in competition with **25** to account for the ∼2:1 (*E*/*Z*) isomer composition of the tracer during the assay.

[^{11}C]9 and [^{18}F]10 PET Biodistribution Studies in Rat. MicroPET measurements were performed on a Siemens MicroPET R4 scanner (Siemens-CTI, Knoxville, TN, USA), which has a spatial resolution at the center of the field of view of 1.84 mm full-width at half-maximum (fwhm) in the axial direction and 1.66 mm fwhm in the radial and tangential directions. The animals were prepared for imaging while under isoflurane (Abbott Laboratories) anesthesia delivered through a nose cone at a concentration of 2.0% volume and 2 L/min oxygen flow; a butterfly cannula (butterfly-25 Short; Venisystems) was placed in the tail vein, and the radiotracer was administered as a 0.2 mL bolus injection. Respiration rate, heart rate, and body temperature were monitored throughout the scan (Biopac systems MP150, Goleta, CA, USA). A 10 min ^{57}Co-transmission scan was acquired to correct for attenuation. Total acquisition time was 90 min. All images were reconstructed using the filtered back projection after applying normalization, scatter corrected for attenuation and radioactivity decay. PET imaging studies were performed in eight (four for each tracer) Sprague−Dawley rats during 2% isoflurane anesthesia. Between 300 and 500 μCi of [^{11}C]**9** or [^{18}F]**10** were injected into the tail vein at the beginning of each scan. Dynamic scans with 27 frames (8 × 30 s, 6 × 60 s, 5 × 120 s, 8 × 300 s) for [^{11}C]**9** and 33 frames (8 × 30 s, 6 × 60 s, 5 × 120 s, 14 × 300 s) for [^{18}F]**10** were acquired over 60 and 90 min, respectively. PET images were reconstructed in a 128 × 128 × 62 matrix with a voxel size of 0.6 mm × 0.6 mm × 1.2 mm using a filtered back projection algorithm with a Hanning filter. For analysis of the [^{11}C]**9** studies, decay corrected brain PET images of radioactivity concentrations [Bq/cc] were analyzed using VINCI 4.07 (Max-Planck-Institute for neurological research, Cologne, http://www.nf.mpg.de/vinci3/). Sum images of all 27 frames were used to place 3D elliptical volumes of interest (VOIs) on brain, lung, and liver. These VOIs were then used to generate time−activity curves from the dynamic scans. Regional radioactivity concentrations [Bq/cc] were converted to standard uptake values relative to bodyweight (SUV_{BW}) and injected dose. For analysis of the [^{18}F]**10** studies, the PET images were analyzed using minctools http://www.bic.mni.mcgill.ca/ServicesSoftware/HomePage). The time−activity curves (TACs) based on regions of interest (ROIs) defined on the rat template were calculated for the following brain regions; cortex, stratum, thalamus, and cerebellum.[62] Uptake of [^{18}F]**10** in the tissues was expressed as standard uptake value (%SUV) calculated as average tissue concentration (MBq/cc) divided by the ratio of injected dose (MBq) over subject mass (grams, with the assumption cc = 1 g) multiplied by 100%.[63]

Animal Experiments. The MicroPET imaging protocol was approved by the Animal Care Committee of McGill University (Montreal, Canada).

■ ASSOCIATED CONTENT

Supporting Information

Conformational equilibrium of **9**, structure of (*E*)- and (*Z*)-**9** and MeOH·(*Z*)-**9**, predicted binding mode of (*E*)-**9** within TrkA, comparison of (*Z*)-**9** binding with TrkB and TrkA, mechanistic explanation for the formation of (*Z*)-[^{11}C]**9** from (*E*)-**16**, UV-visible spectra changes upon treatment **9** (*E*/*Z* mixture) with $NaOH_{(aq)}$, predicted sites of metabolism using IMPACT for (*Z*)-**9**, HPLC chromatograms over 90 min for the RLM assay with (*E*/*Z*)-**9** and (*E*/*Z*)-**10**, ^{1}H-NMR spectra at different time points during photoisomerization of (*Z*)-**10**, LC-MS/MS analysis of the **10** *E*/*Z* mixture, dose−response curves for the [γ-^{33}P]ATP-based enzymatic *in vitro* assays of TrkA, TrkB, and TrkC with **16**, **10**, and **18a**−**e**, autoradiography of human neuroblastoma tumors with [^{18}F]**10** alone and in co-incubation with inhibitors **3**, mechanistic rationale for synthesis of (*Z*)-**9**, chemical synthesis of 2-fluoroethyl 4-methylbenzenesulfonate, and crystallographic data for compounds **12** and (*Z*)-

9. This material is available free of charge via the Internet at http://pubs.acs.org.

AUTHOR INFORMATION

Corresponding Authors

*Prof. R. Schirrmacher. Fax: (+1) 514-340-7502; E-mail: schirrma@ualberta.ca.

*Vadim Bernard-Gauthier. E-mail: vadim.bernard-gauthier@mail.mcgill.ca.

Author Contributions

Vadim Bernard-Gauthier: study conception and design, acquisition of data (chemistry, radiochemistry, metabolism studies, *in silico* studies, autoradiography), analysis and interpretation of data (chemistry, radiochemistry, metabolism studies, *in silico* studies, autoradiography, PET studies), writing of manuscript, corrections, and revision. Arturo Aliaga: acquisition of data (autoradiography), data analysis (autoradiography). Antonio Aliaga: acquisition of data (PET), data analysis (PET). Mehdi Boudjemeline: acquisition of data (chemistry). Robert Hopewell: acquisition of data (radiochemistry). Alexey Kostikov: acquisition of data (radiochemistry). Pedro Rosa-Neto: acquisition of data (autoradiography). Alexander Thiel: data analysis (PET). Ralf Schirrmacher: study conception and design, corrections, and revision.

Funding

This work was financially supported by Canada Foundation for Innovation (CFI) Project No. 203639 to R.S.

Notes

The authors declare no competing financial interest.

ACKNOWLEDGMENTS

We thank Dr. Esther Schirrmacher for reading the manuscript and providing useful comments. We are thankful to Dr. Hervé Sartelet who courteously provided human neuroblastoma samples for autoradiography experiments. We thank Marilyn Grand'Maison for the valuable help for the preparation of figures and histological staining. We thank Antonio Aliaga for small animal PET imaging and Arturo Aliaga for autoradiography experiments. We are also grateful to Dean Jolly and Miriam M. Kovacevic for radioisotope production. We thank Ming-Kai Ho for the digitalization of the histological staining sections. We thank Dr. Perrine Gaub for western blot analysis.

REFERENCES

(1) Pattarawarapan, M., and Burgess, K. (2003) Molecular basis of neurotrophin-receptor interactions. *J. Med. Chem. 46*, 5277−5291.

(2) Schneider, R., and Schweiger, M. (1991) A novel modular mosaic of cell adhesion motifs in the extracellular domains of the neurogenic trk and trkB tyrosine kinase receptors. *Oncogene 6*, 1807−1811.

(3) Huang, E. J., and Reichardt, L. F. (2001) Neurotrophins: Roles in neuronal development and function. *Annu. Rev. Neurosci. 24*, 677−736.

(4) Huang, E. J., and Reichardt, L. F. (2003) Trk receptors: Roles in neuronal signal transduction. *Annu. Rev. Neurosci. 72*, 609−642.

(5) Chao, M. V. (2003) Neurotrophins and their receptors: A convergence point for many signalling pathways. *Nat. Rev. Neurosci. 4*, 299−309.

(6) Snider, W. D. (1994) Functions of the neurotrophins during nervous system development: what the knockouts are teaching us. *Cell 77*, 627−638.

(7) Chao, M. V., and Hempstead, B. L. (1995) p75 and Trk: A two receptor system. *Trends Neurosci. 18*, 321−326.

(8) Kaplan, D. N., Martin-Zanca, D., and Parada, L. F. (1991) Tyrosine phosphorylation and tyrosine kinase activity of the trk proto-oncogene product induced by NGF. *Nature 350*, 158−160.

(9) Holtzman, D. M., Kilbridge, J., Li, Y., Cunningham, E. T., Lenn, N. J., Clary, D., Reichardt, L. F., and Mobley, W. C. (1995) TrkA expression in the CNS: Evidence for the existence of several novel NGF-responsive CNS neurons. *J. Neurosci. 15*, 1567−1576.

(10) Muragaki, Y., Timothy, N., Leight, S., Hempstead, B. L., Chao, M. V., Trojanowsaki, J. Q., and Lee, V. M. (1995) Expression of trk receptors in the developing and adult human central and peripheral nervous system. *J. Comp. Neurol. 356*, 387−397.

(11) Tessarollo, L., Tsoulfas, P., Martin-Zanca, D., Gilbert, D. J., Jenkins, N. A., Copeland, N. G., and Parada, L. F. (1993) *trk*C, a receptor for neurotrophin-3, is widely expressed in the developing nervous system and in non-neuronal tissues. *Development 118*, 463−475.

(12) Shibayama, E., and Koizumi, H. (1996) Cellular localization of the Trk neurotrophin receptor family in human non-neuronal tissues. *Am. J. Pathol. 148*, 1807−1818.

(13) (a) Gupta, V. K., You, Y., Gupta, V. B., Klistorner, A., and Graham, S. L. (2013) TrkB receptor signaling: Implication in neurodegenerative, psychiatric and prolifertive disorders. *Int. J. Mol. Sci.*, 10122−10143. (b) Cattaneo, A., and Calissano, P. (2012) Nerve growth factor and Alzheimer's Disease: new facts for an old hypothesis. *Mol. Neurobiol. 46*, 588−604.

(14) Sanchez-Ortiz, E., Yui, D., Song, D., Li, Y., Rubenstein, J. L., Reichardt, L. F., and Parada, L. F. (2012) TrkA gene ablation in basal forebrain results in dysfunction of the cholinergic circuitry. *J. Neurosci. 32*, 4065−4079.

(15) Scott, S. A., Mufson, E. J., Weingartner, J. A., Skau, K. A., and Crutcher, K. A. (1995) Nerve growth factor in Alzheimer's disease: Increased levels throughout the brain coupled with declines in nucleus basalis. *J. Neurosci. 15*, 6213−6221.

(16) (a) Ginsberg, S. D., Che, S., Wuu, J., Counts, S. E., and Mufson, E. J. (2006) Down regulation of trk but not p75NTR gene expression in single cholinergic basal forebrain neurons mark the progression of Alzheimer's disease. *J. Neurochem. 97*, 475−487. (b) Mufson, E. J., Li, J. M., Sobreviela, T., and Kordower, J. H. (1996) Decreased trkA gene expression within basal forebrain neurons in Alzheimer's disease. *Neuroreport 20*, 25−29.

(17) Mufson, E. J., Count, S. E., Fahnestock, M., and Ginsberg, S. D. (2007) Cholinotrophic molecular substrates of mild cognitive impairment in the ederly. *Curr. Alzheimer Res. 4*, 340−350.

(18) Counts, S. E., Nadeem, M., Wuu, J., Ginsberg, S. D., Saragovi, H. U., and Mufson, E. J. (2004) Reduction of cortical TrkA but not $p75^{NTR}$ protein in early-stage Alzheimer's disease. *Ann. Neurol. 56*, 520−531.

(19) Ferrer, I., Marin, C., Rey, M. J., Ribalta, T., Goutan, E., Blanco, R., Tolosa, E., and Marti, E. (1999) BDNF and full-length and truncated TrkB expression in Alzheimer disease. Implication in therapeutic strategies. *J. Neuropathol. Exp. Neurol. 58*, 729−739.

(20) Fumagalli, F., Racagni, G., and Riva, M. A. (2006) Shedding light into the role of BDNF in the pharmacotherapy of Parkinson's disease. *Pharmacogenomics 6*, 95−104.

(21) Zuccato, C., Marullo, M., Conforti, P., MacDonald, M. E., Tartari, M., and Cattaneo, E. (2008) Systematic assessment of BDNF and its receptor levels in human cortices affected by Huntington's disease. *Brain Pathol. 18*, 225−238.

(22) Pillai, A. (2008) Brain-derived neurotropic factor/TrkB signaling in the pathogenesis and novel pharmacotherapy of schizophrenia. *Neurosignals 16*, 183−193.

(23) Griesbach, G. S., Hovda, D. A., and Gomez-Pinilla, F. (2009) Exercise-induced improvement in cognitive performance after traumatic brain injury in rats is dependent on BDNF activation. *Brain Res. 1288*, 105−115.

(24) Sclabas, G. M., Fujioka, S., Schmidt, C., Li, Z., Frederick, W. A. I., Yang, Y., Yokoi, K., Evans, D. B., Abbruzzese, J. L., Hess, K. R., Zhang, W., Fidler, I. J., and Chiao, P. J. (2005) Overexpression of

tropomysin-related kinase B in metastatic human pancreatic cancer cells. *Clin. Cancer Res. 11*, 440−449.
(25) Okamura, K., Harada, T., Wang, S., Ijichi, K., Furuyama, K., Koga, T., Okamoto, T., Takayama, K., Yano, T., and Nakanishi, Y. (2012) Expression of TrkB and BDNF is associated with poor prognosis in non-small cell lung cancer. *Lung Cancer 78*, 100−106.
(26) Hisaoka, M., Sheng, W. Q., Tanaka, A., and Hashimoto, H. (2002) Gene expression of TrkC (NTRK3) in human soft tissue tumours. *J. Pathol. 197*, 661−667.
(27) Geiger, T. R., and Peeper, D. S. (2005) The neurotrophic receptor TrkB in anoikis resistance and metastasis: A Perspective. *Cancer Res. 65*, 7033−7036.
(28) (a) Nakagawara, A., Azar, C. G., Scavarda, N. J., and Brodeur, G. M. (1994) Expression and function of TRK-B and BDNF in human neuroblastomasExpression and function of TRK-B and BDNF in human neuroblastomas.Expression and function of TRK-B and BDNF in human neuroblastomas. *Mol. Cell. Biol. 14*, 759−767.
(29) Longo, F. M., and Massa, S. M. (2013) Small-molecule modulation of neurotrophin receptors: A strategy for the treatment of neurological disease. *Nat. Rev. Drug Discovery 12*, 507−525.
(30) Wang, T., Yu, D., and Lamb, M. L. (2009) Trk kinase inhibitors as new treatments for cancer and pain. *Expert Opin. Ther. Pat. 19*, 305−319.
(31) (a) Carzola, M., Premont, J., Girard, N., Kellendonk, C., and Rognan, D. (2011) Identification of a low-molecular weight TrkB antagonist with anxiolytic and antidepressant activity in mice. *J. Clin. Invest. 121*, 1846−1857. (b) Massa, S. M., Yang, T., Xie, Y., Shi, J., Bilgen, M., Joyce, J. N., Nehama, D., Rajadas, J., and Longo, F. M. (2010) Small molecules BDNF mimetics activate TrkB signaling and prevent neuronal degeneration in rodents. *J. Clin. Invest. 120*, 1774−1785. (c) Pattarawarapan, M., Zaccaro, M. C., Saragovi, U. H., and Burgess, K. (2002) New templates for syntheses of ring-fused, C10 β-turn peprtidomimetics leading to the first reported small-molecule mimic of neurotrophin-3. *J. Med. Chem. 45*, 4387−4390.
(32) (a) Jang, S.-W., Liu, X., Yepes, M., Shepherd, K. R., Miller, G. W., Liu, Y., Wilson, W. D., Xiao, G., Blanchi, B., Sun, Y., and Ye, K. (2010) A selective TrkB agonist with potent neurotrophic activities by 7,8-dihydroxyflavone. *Proc. Natl. Acad. Sci. U.S.A. 107*, 2687−2692. (b) Liu, X., Chan, C.-B., Jang, S.-W., Pradoldej, S., Huang, J., He, K., Phun, L. H., France, S., Xiao, G., Jia, Y., Luo, H. R., and Ye, K. (2010) A Synthetic 7,8-dihydroxyflavone derivative promotes neurogenesis and exhibits potent antidepressant effect. *J. Med. Chem. 53*, 8274−8286. (c) Liu, X., Chan, C.-B., Qi, Q., Xiao, G., Luo, H. R., He, X., and Ye, K. (2012) Optimization of a small tropomyosin-related kinase B (TrkB) agonist 7,8-dihydroxyflavone active in mouse models of depression. *J. Med. Chem. 55*, 8524−8537.
(33) Hong, S., Kim, J., Seo, J. H., Jung, K. H., Hong, S.-S., and Hong, S. (2012) Design, synthesis, and evaluation of 3,5-disustituted 7-azaindoles as Trk inhibitors with anticancer and antiangiogenic activities. *J. Med. Chem. 55*, 5337−5349.
(34) Lippa, B., Morris, J., Corbett, M., Kwan, T. A., Noe, M. C., Snow, S. L., Gant, T. G., Mangiaracina, M., Coffey, H. A., Foster, B., Knauth, E. A., and Wessel, M. D. (2006) Discovery of novel isothiazole inhibitors of the TrkA kinase: structure-activity relationship, computer modeling, optimization, and identification of highly potent antagonist. *Bioorg. Med. Chem. Lett. 16*, 3444−3448.
(35) Kim, S.-H., Tokarski, J. S., Leavitt, K. J., Fink, B. E., Salvati, M. E., Moquin, R., Obermeier, M. T., Trainor, G. L., Vite, G. G., Stadnick, L. K., Lippy, J. S., You, D., Lorenzi, M. V., and Chen, P. (2008) Identification of 2-amino-5-(thioaryl)-thiazoles as inhibitors of the nerve growth factor receptor TrkA. *Bioorg. Med. Chem. Lett. 18*, 634−639.
(36) See, for example: Albaugh, P., Fan, Y., Mi, Y., Sun, F., Adrian, F., Li, N., Jia, Y., Sarkisova, Y., Kreusch, A., Hood, T., Lu, M., Liu, G., Huang, S., Liu, Z., Loren, J., Tuntland, T., Karanewsky, D. S., Martin Seidel, H., and Molteni, V. (2012) Discovery of GNF-5839, a selective Trk inhibitor with efficacy in rodent cancer tumor models. *ACS Med. Chem. Lett. 3*, 140−145.
(37) Bernard-Gauthier, V., Boudjemeline, M., Rosa-Neto, P., Thiel, A., and Schirrmacher, R. (2013) Towards tropomyosin-related kinase B (TrkB) receptor ligands for brain imaging with PET: Radiosynthesis and evaluation of 2-(4-[^{18}F]fluorophenyl)-7,8-dihydroxy-4*H*-chromen-4-one and 2-(4-([*N*-methyl-^{11}C]-dimethylamino)phenyl)-7,8-dihydroxy-4*H*-chromen-4-one. *Bioorg. Med. Chem. 21*, 7816−7829.
(38) Altar, C. A., Siuciak, J. A., Wright, P., Ip, N. Y., Lindsay, R. M., and Wiegand, S. J. (1994) In situ hybridization of TrkB and TrkC receptor mRNA in rat forebrain and association with high-affinity binding of [125I]BDNF, [125I]NT-4/5 and [125I]NT-3. *Eur. J. Neurosci. 6*, 1389−1405.
(39) Zhang, L., Villalobos, A., Beck, E. M., Bocan, T., Chappie, T. A., Chen, L., Grimwood, S., Heck, S. D., Helal, C. J., Hou, X., Humphrey, J. M., Lu, J., Skaddan, M. B., McCarthy, T. J., Verhoest, P. R., Wager, T. T., and Zasadny, K. (2013) Design and selection parameters to accelerate the discovery of novel central nervous system positron emission tomography (PET) ligands and their application in the development of a novel phosphodiesterase 2A PET ligand. *J. Med. Chem. 56*, 4568−4579.
(40) Pike, V. W. (2009) PET radiotracers: Crossing the blood−brain barrier and surviving metabolism. *Trends Pharmacol. Sci. 30*, 431−440.
(41) Wood, E. R., Kuyper, L., Petrov, K. G., Hunter, R. N., Harris, P. A., and Lackey, K. (2006) Discovery and in vitro evaluation of potent TrkA kinase inhibitors: Oxindole and aza-oxindoles. *Bioorg. Med. Chem. Lett. 14*, 953−957.
(42) Altar, C. A., Criden, M. R., Lindsay, R. M., and DiStefano, P. S. (1993) Characterization and topography of high-affinity 1251-neurotrophin-3 binding to mammalian brain. *J. Neurosci. 13*, 733−743.
(43) (a) Zou, H., Zhang, L., Ouyang, J., Giulianotti, M. A., and Yu, Y. (2011) Synthesis and biological evaluation of 2-indolinone derivatives as potential antitumor agents. *Eur. J. Med. Chem. 46*, 5970−5977. (b) Liu, J.-J., Dermatakis, A., Lukacs, C., Konzelmann, F., Chen, Y., Kammlott, U., Depinto, W., Yang, H., Yin, X., Chen, Y., Schutt, A., Simcox, M. E., and Luk, K.- C. (2003) 3,5,6-Trisubstituted naphthostyrils as CDK2 inhibitors. *Bioorg. Med. Chem. Lett. 13*, 2465−2468. (c) Laufer, R., Forrest, B., Li, S.-W., Liu, Y., Sampson, P., Edwards, L., Lang, Y., Awrey, D. E., Mao, G., Plotnikova, O., Leung, G., Hodgson, R., Beletskaya, I., Mason, J. M., Luo, X., Wei, X., Yao, Y., Feher, M., Ban, F., Kiarash, R., Green, E., Mak, T. W., Pan, G., and Pauls, H. W. (2013) The discovery of PLK4 inhibitors: (*E*)-3-((1*H*-Indazol-6-yl)methylene)indolin-2-ones as novel antiproliferative agents. *J. Med. Chem. 56*, 6069−6087. For review, see: (d) Prakash, C. R., Theivendren, P., and Raja, S. (2012) Indolin-2-ones in clinical trials as potential kinase inhibitors: A review. *Pharmacol. Pharm. 3*, 62−71.
(44) Sun, L., Tran, N., Tang, F., App, H., Hirth, P., McMahon, G., and Tang, C. (1998) Synthesis and biological evaluations of 3-substituted indolin-2-ones: A novel class of tyrosine kinase inhibitors that exhibit selectivity toward particular receptor tyrosine kinases. *J. Med. Chem. 41*, 2588−2603.
(45) Bertrand, T., Kothe, M., Liu, J., Dupuy, A., Rak, A., Berne, P. F., Davis, S., Gladysheva, T., Valtre, C., Crenne, J. Y., and Mathieu, M. (2012) The crystal structures of TrkA and TrkB suggests key regions for achieving selective inhibition. *J. Mol. Biol. 423*, 439−453.
(46) (a) Englebienne, P., and Moitessier, N. (2009) Docking ligands into flexible and solvated macromolecules. 5. Force-field-based prediction of binding affinities of ligands to proteins. *J. Chem. Inf. Model 49*, 2564−2571. (b) Therrien, E., Englebienne, P., Arrowsmith, A. G., Mendoza-Sanchez, R., Corbeil, C. R., Weill, N., Campagna-Slater, V., and Moitessier, N. (2012) Integrating medicinal chemistry, organic/combinatorial chemistry, and computational chemistry for the discovery of selective estrogen receptor modulators with FORECASTER, a novel platform for drug discovery. *J. Chem. Inf. Model 52*, 210−224. (c) Corbeil, C. R., Englebienne, P., Yannopoulos, C. G., Chan, L., Das, S. K., Bilimoria, D., L'Heureux, L., and Moitessier, N. (2008) Docking ligands into flexible and solvated macromolecules. 2. Development and application of FITTED 1.5 to the virtual screening of potential HCV polymerase inhibitors. *J. Chem. Inf. Model 48*, 902−909.

(47) (a) Mologhia, L., Rostagnoa, R., Brussolo, S., Knowles, P. P., Kjaer, S., Murray-Rust, J., Rosso, E., Zambonb, A., Scapozza, L., McDonald, N. Q., Lucchini, V., and Gambacorti-Passerini, C. (2010) Synthesis, structure−activity relationship and crystallographic studies of 3-substituted indolin-2-one RET inhibitors. *Bioorg. Med. Chem. 18*, 1482−1496. (b) Bramson, H. N., Corona, J., Davis, S. T., Dickerson, S. H., Edelstein, M., Frye, S. V., Gampe, R. T., Harris, P. A., Hassell, A., Holmes, W. D., Hunter, R. N., Lackey, K. E., Lovejoy, B., Luzzio, M. J., Montana, V., Rocque, W. J., Rusnak, D., Shewchuk, L., Veal, J. M., Walker, D. H., and Kuyper, L. F. (2001) Oxindole-based inhibitors of cyclin-dependent kinase 2 (CDK2): design, synthesis, enzymatic activities, and X-ray crystallographic analysis. *J. Med. Chem. 44*, 4339−4358. (c) Gajiwala, K. S., Wu, J. C., Christensen, J., Deshmukh, G. D., Diehl, W., Dinitto, J. P., English, J. M., Greig, M. J., He, Y.-A., Jacques, S. L., Lunney, E. A., McTigue, M., Molina, D., Quenzer, T., Wells, P. A., Yu, X., Zhang, Y., Zou, A., Emmette, M. R., Marshall, A. G., Zhang, H.-M., and Demetri, G. M. (2009) KIT kinase mutants show unique mechanisms of drug resistance to imatinib and sunitinib in gastrointestinal stromal tumor patients. *Proc. Natl. Acad. Sci. U.S.A. 106*, 1542−1547. (d) Mohammadi, M., McMahon, G., Sun, L., Tang, C., Hirth, P., Yeh, B. K., Hubbard, S. R., and Schlessinger, J. (1997) Structures of the tyrosine kinase domain of fibroblast growth factor receptor in complex with inhibitors. *Science 276*, 955−960.

(48) Mashhoon, N., DeMaggio, A. J., Tereshko, V., Bergmeieri, S. C., Egli, M., Hoekstra, M. F., and Kuret, J. (2000) Crystal structure of a conformation-selective casein kinase-1 inhibitor. *J. Biol. Chem. 275*, 20052−20060.

(49) Sarkisyan, K. S., Yampolsky, I. V., Slontsev, K. M., Lukyanov, S. A., Lukyanov, K. A., and Mishin, A. S. (2012) Tryptophan-based chromophore in fluorescent proteins ca be anionic. *Sci. Rep. 2*, No. 608.

(50) Campagna-Slater, V., Pottel, J., Therrien, E., Cantin, L.-D., and Moitessier, N. (2012) Development of a computational tool to rival experts in the prediction of sites of metabolism of xenobiotics by P450s. *J. Chem. Inf. Model. 52*, 2471−2483.

(51) (a) Martignoni, M., Groothuis, G. M. M., and de Kanter, R. (2006) Species differences between mouse, rat, dog, monkey and human CYP-mediated drug metabolism, inhibition and induction. *Expert Opin. Drug Metab. Toxicol. 2*, 875−894. (b) Wilkinson, G. R. (2005) Drug metabolism and variability among patients in drug response. *N. Engl. J. Med. 352*, 2211−2221.

(52) Altar, A. C., Burton, L. E., Bennett, G. L., and Dugich-Djordjevic, M. (1991) Neurobiology recombinant human nerve growth factor is biologically active and labels novel high-affinity binding sites in rat brain. *Proc. Natl. Acad. Sci. U. S. A. 88*, 281−285.

(53) (a) Nakagawara, A., Azar, C. G., Scavarda, N. J., and Brodeur, G. M. (1994) Expression and function of TRK-B and BDNF in human neuroblastomas. *Mol. Cell. Biol. 14*, 759−767. (b) Matsumoto, K., Wada, R. K., Yamashiro, J. M., Kaplan, D. R., and Thiele, C. J. (1995) Expression of brain-derived neurotrophic factor and $p145^{TrkB}$ affects survival, differentiation, and invasiveness of human neuroblastoma cells. *Cancer Res. 55*, 1798−1806. For review, see: (c) Brodeur, G. M., Minturn, J. E., Ho, R., Simpson, A. M., Iyer, R., Varela, C. R., Light, J. E., Kolla, V., and Evans, A. E. (2009) Trk Receptor Expression and inhibition in neuroblastomas. *Clin. Cancer Res. 15*, 3244−3250.

(54) (a) Ricci, A., Felici, L., Mariotta, S., Mannino, F., Schmid, G., Terzano, C., Cardillo, G., Amenta, F., and Bronzetti, E. (2004) Neurotrophin and neurotrophin receptor protein expression in the human lung. *Am. J. Respir. Cell Mol. Biol. 30*, 12−19. (b) Garcia-Suárez, O., Pérez-Pinera, P., Laurà, R., Germana, A., Esteban, I., Cabo, R., Silos-Santiago, I., Cobo, J. L., and Vega, J. A. (2009) TrkB is necessary for the normal development of the lung. *Respir. Physiol. Neurobiol. 167*, 281−291.

(55) Raab, S., and Plate, K. H. (2007) Different networks, common growth factors: Shared growth factors and receptors of the vascular and nervous system. *Acta Neuropathol. 113*, 607−626.

(56) Coffey, E. T. (2014) Nuclear and cytosolic JNK signaling in neurons. *Nat. Rev. Neurosci. 15*, 285−299.

(57) Ingraham, C. A., Cox, M. E., Ward, D. C., Fults, D. W., and Maness, P. F. (1989) C-SRC and other proto-oncogenes implicated in neuronal differentiation. *Mol. Chem. Neuropathol. 1*, 1−14.

(58) Iwahara, T., Fujimoto, J., Cupples, R., Bucay, N., Arakawa, T., Mori, S., Ratzkin, B., and Yamamoto, T. (1997) Molecular charaterization of ALK, a receptor tyrosine kinase expressed specifically in the nervous system. *Oncogene 14*, 439−449.

(59) Achim, C. L., Katyal, S., Wiley, C. A., Shiratori, M., Wang, G., Oshika, E., Petersen, B. E., Li, J.-M., and Michalopoulos, G. K. (1997) Expression of HGF and cMet in the developing and adult brain. *Dev. Brain Res. 102*, 299−303.

(60) Block, D., Coenen, H. H., and Stöcklin, G. (1987) The n.c.a. nucleophilic ^{18}F-fluorination of 1,*N*-disubstitutedalkanes as fluoralkylation agents. *J. Labelled Compd. Radiopharm. 24*, 1029−1042.

(61) Zoghbi, S. S., Shetty, U., Ichise, M., Fujita, M., Imaizumi, M., Liow, J.-S., Shah, J., Musachio, J. L., Pike, V. W., and Innis, R. B. (2006) PET imaging of the dopamine transporter with 18F-FECNT: A polar radiometabolite confounds brain radioligand measurements. *J. Nucl. Med. 47*, 520−527.

(62) Parent, M., Bedard, M. A., Aliaga, A., Soucy, J. P., Landry St-Pierre, E., Cyr, M., Kostikov, A., Schirrmacher, E., Massarweh, G., and Rosa-Neto, P. (2012) PET imaging of cholinergic deficits in rats using [^{18}F]fluoroethoxybenzovesamicol ([^{18}F]FEOBV). *NeuroImage 62*, 555−561.

(63) Aliaga, A., Rousseau, J. A., Cadorette, J., Croteau, E., van Lier, J. E., Lecomte, R., and Bénard, F. (2007) A small animal positron emission tomography study of the effect of chemotherapy and hormonal therapy on the uptake of 2-deoxy-2-[F-18]fluoro-d-glucose in murine models of breast cancer. *Mol. Imaging Biol. 9*, 144−150.